Genetic Relationship between Subduction of Slab Topographic Anomalies and Porphyry Deposit Formation: Insight from the Source and Evolution of Rio Blanco Magmas

Nian Chen[1], Xuyang Meng[2,*], Jingwen Mao[1,3,*] and Guiqing Xie[1,3]

[1]MNR Key Laboratory for Exploration Theory & Technology of Critical Mineral Resources, China University of Geosciences, 29# Xueyuan Road, Haidian District, Beijing 100083, China
[2]Department of Earth and Environmental Sciences, University of Michigan, 1100 North University Avenue Ann Arbor, MI 48109, USA
[3]Ministry of Natural Resources (MNR) Key Laboratory of Metallogeny and Mineral Assessment, Institute of Mineral Resources, Chinese Academy of Geological Sciences (CAGS), 26# Baiwanzhuang Street, Xicheng District, Beijing 100037, China

*Corresponding author. E-mail: xuyangm@umich.edu (Xuyang Meng); jingwenmao@263.net (Jingwen Mao)

Abstract

The Rio Blanco deposit, which is one of the largest porphyry Cu–Mo deposits in northern Peru, formed coevally with the subduction of the Inca Oceanic Plateau at 12–10 Ma. However, the genetic relationship between the subduction of oceanic plateaus and the porphyry deposit formation remains unclear. Igneous rocks emplaced at 23–12 Ma in northern Peru, including the Portachuela batholith (which hosts the Rio Blanco porphyry complex), are normal calc-alkaline to weakly adakitic. In comparison, the 12–8 Ma igneous rocks, including the ore-related Rio Blanco porphyry complex, have typical adakitic signatures, such as high Sr/Y ratios (up to 180) and La_N/Yb_N ratios (up to 32). The Rio Blanco igneous rocks (Portachuela batholith and Rio Blanco porphyry complex) have uniform zircon $\varepsilon_{Hf}(t)$ values ($+0.3 \pm 1.2$) and $\delta^{18}O$ values (6.5 ± 0.14‰). These geochemical characteristics indicate that the Rio Blanco igneous rocks evolved from mantle-derived parental melts in a long-lived, stable, homogeneous isotopic reservoir at the crust–mantle boundary. However, whereas both the Portachuela batholith and the Rio Blanco porphyry complex formed from hydrous parental magmas (>5 wt %; based on plagioclase hygrometry), the ones of the Rio Blanco porphyry complex seem to be more oxidized, hydrous, and sulfur-rich compared with the older batholitic rocks. Reverse zoning in plagioclase phenocrysts, with a systematic core–mantle–rim variation in An (anorthite) and Fe (total iron) contents, are common in the intermineralization rocks. The An content of the mantles of the plagioclase phenocrysts correlates positively with the Fe content, but in the rims, the An contents significantly decrease while Fe remains constant. The apatite inclusions in the mantles are richer in S (0.24 ± 0.06 wt %) and Cl (1.42 ± 0.32 wt %) than those in the phenocryst cores (S: 0.09 ± 0.07 wt %; Cl: 1.03 ± 0.56 wt %) and rims (S: 0.14 ± 0.09 wt %; Cl: 0.83 ± 0.35 wt %). These systemic geochemical variations in the plagioclase phenocrysts suggest recharge by S- and Cl-rich melts followed by fluid exsolution. This magma recharge and subsequent fluid exsolution may have triggered porphyry Cu mineralization at Rio Blanco. The coincidence of timing between the geochemical transition and collision (initial subduction) of the Inca Oceanic Plateau with the South American plate may indicate a change in the tectonic regime to a compressional state of stress and a thickening of the crust during the collision. The tectonic transition would have facilitated the fractionation of mantle-derived magma in a deep crustal hot zone, resulting in oxidized, volatile-rich residual melts. Replenishment of the upper-crustal magma chamber by such volatile-rich magmas and the subsequent discharge of fluids are interpreted to be fundamental for porphyry Cu mineralization at Rio Blanco and plausibly for the formation of Late Miocene porphyry ore deposits in northern Peru in general.

Keywords: northern Peru, Inca Oceanic Plateau, volatile-rich melt recharge, Rio Blanco porphyry deposit

INTRODUCTION

Porphyry Cu systems are presently the main sources of Cu and Mo around the world (Sillitoe, 2010). The associated calc-alkaline to mildly alkalic magmas are relatively oxidized and volatile-rich, and many of them have adakitic geochemical characteristics (Rohrlach & Loucks, 2005; Richards, 2011a; Richards et al., 2012; Loucks, 2014, 2021; Chiaradia, 2015). These geochemical features may result from a series of processes operating in subduction zones at convergent continental margins, including (1) slab-derived fluids metasomatizing mantle wedges, decreasing their solidus temperature, and triggering partial melting; (2) underplating of mantle-derived basaltic melts at the base of the crust (experienced processes of melting, assimilation, storage, and homogenization), thus forming andesitic melts; and (3) subsequent fractional crystallization and crustal contamination during magma ascent to mid- to upper-crustal reservoirs (Hildreth & Moorbath, 1988; Defant & Drummond, 1990; Bourdon et al., 2002; Zhang et al., 2006; Chiaradia et al., 2009a; Munoz et al., 2012; Mao et al., 2014; Cashman et al., 2017; Cheng et al., 2018).

Extensive convergent margin magmatism has been ongoing since the Late Oligocene in the north Central Andes (Coira et al., 1982; Pilger, 1984; Jaillard et al., 2000). The time and space restriction of giant porphyry Cu deposits suggests that these deposits formed under atypical tectonomagmatic conditions in a restricted arc segment since the Late Oligocene (Tosdal & Richards, 2001; Richards, 2003, 2013; Cooke et al., 2005; Rosenbaum et al., 2005; Sillitoe & Perelló, 2005; Wilkinson, 2013). Many studies suggest that the porphyry Cu deposits in the South American Andes are commonly associated with topographic anomalies on subducted oceanic crust, such as oceanic plateaus, oceanic ridges, and island chains (Cooke et al., 2005; Rosenbaum et al., 2005; Sun et al., 2010). The subduction of a topographic anomaly increases coupling between two plates, resulting in enhanced crustal stress and crustal thickness (Kay & Mpodozis, 2001; Rosenbaum et al., 2005; Chiaradia et al., 2009a ; Loucks, 2021), which may reduce magmatic ascent or supply rates (Skewes & Stern, 1994; Stern & Skewes, 2005; Chiaradia et al., 2009a). Arc compression contributes to prolonged magmatic evolution (Farner & Lee, 2017) and maturation at variable crustal levels and promotes fertility (high fO_2 and volatile content) of the magmas for porphyry mineralization (Chiaradia et al., 2009a; Loucks, 2021). Meanwhile, recent studies propose that formation of the porphyry Cu deposits in the Andes are associated with elevated magma fluxes (Caricchi et al., 2014; Schöpa et al., 2017; Cox et al., 2020). Although several petrogenetic studies have attempted to address the genetic relationship between the subduction of topographic anomalies and the formation of porphyry deposits (e.g. Reich et al., 2003; Hollings et al., 2005; Chiaradia et al., 2009a; Carrasquero et al., 2018), the optimal geochemical conditions associated with such subduction for the formation of porphyry ore systems remain unclear.

The Rio Blanco porphyry deposit formed at ca. 11.2 Ma (Chen et al., 2022), coeval with the initial subduction of the Inca Oceanic Plateau (12–10 Ma; Fig. 1; Gutscher et al., 1999). Therefore, it is an ideal location for investigating the genetic relationship between the subduction of topographic anomalies and the formation of porphyry deposits. Note that subduction of topographic anomaly is a period including (1) the initial subduction (we define as 'collision' here) of a topographic anomaly at subduction trench and (2) the subsequent flat-slab subduction into the trench.

Here we present a geochemical and mineralogical study of the Portachuela batholith and Rio Blanco porphyry complex, located 40 km northeast of the Huancabamba Province, Piura region, northern Peru (Fig. 1c). We also compare our results in a regional context to previously published elemental and isotopic data for Miocene igneous rocks in northern Peru. This study aims to (1) determine the source and evolution processes of magmatism in the Rio Blanco district and (2) investigate the possible genetic relationship between

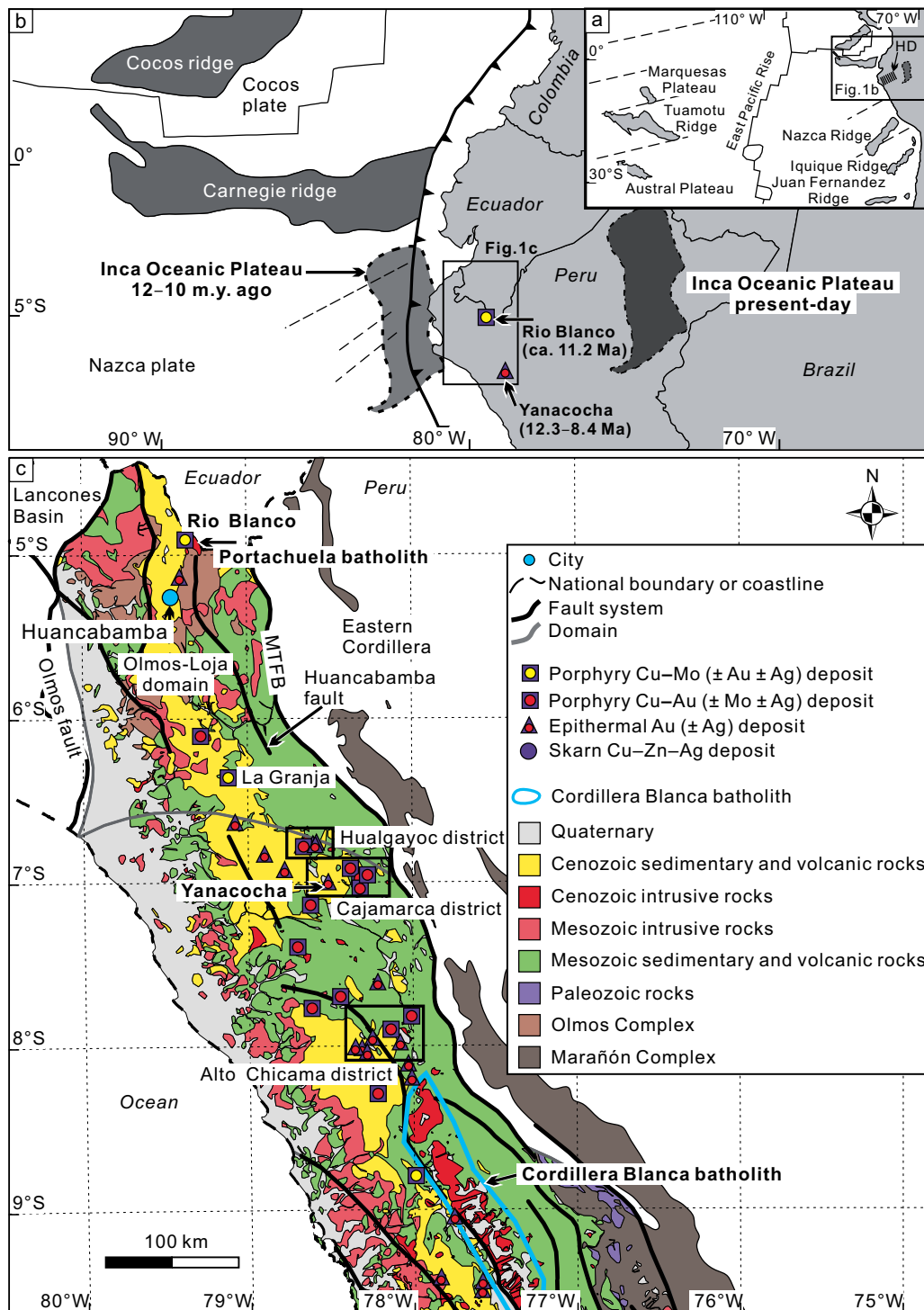the subduction of the Inca Oceanic Plateau and the formation of the Rio Blanco porphyry Cu–Mo deposit.

GEOLOGICAL SETTING
Geology and magmatism in northern Peru
Rio Blanco is located in northernmost Peru (Fig. 1a and b), where the Huancabamba deflection marks the change in orientation of the Andean chain from a NW trend in the south to a NE trend in the north (Fig. 1a; Mourier et al., 1988; Jaillard et al., 2000; Pilatasig et al., 2005). Three major fault systems are located from west to east in this region (Fig. 1c), including (1) the Olmos fault, separating the Lancones basin and the Olmos-Loja domain; (2) the Huancabamba fault in the central sector; and (3) the Marañón thrust and fold belt (MTFB), bounding the Eastern Cordillera (Mégard et al., 1984). The oblique subduction during the Oligocene and Early Miocene resulted in dextral shearing (Kennan & Pindell, 2009).

The basement of northern Peru is composed mainly of the Marañón Complex and Olmos Complex (Fig. 1c). The Marañón Complex is cropped out mainly to the east of the MTFB and consists of Precambrian–Paleozoic gneisses and schists (Cardona et al., 2006, 2009; Chew et al., 2007, 2016; Ramos, 2010). The Paleozoic quartzites and phyllites of the Olmos Complex, which are exposed in the Olmos-Loja domain, are the dominant basement rocks at Rio Blanco (Feininger, 1982; Luis & Julio, 1987; Litherland et al., 1994; Chew et al., 2007; Luis & Julio, 2017). These basement rocks are unconformably overlain by Jurassic–Cretaceous platform sequences and volcanic deposits (James, 1995; Longridge, 2016). Cenozoic fluvial and volcanic deposits overlie Mesozoic sequences along an angular unconformity (Beas, 2015; Longridge, 2016).

Miocene magmatism in northern Peru commenced with the Quechua I orogeny (ca. 23 Ma; Noble et al., 1990; Longo et al., 2005), simultaneous with the breakup of the Farallon plate into the Nazca and Cocos plates (Lonsdale, 2005). The convergence rate abruptly increased from 5–8 cm/yr to ca. 15 cm/yr, and the NE–SW convergence rotated toward the E–W direction (Somoza, 1998; Somoza & Ghidella, 2012). This orogenic event caused structural deformation and magmatism during the Early Miocene in northern Peru (McKee & Noble, 1982; Mégard, 1984; Noble et al., 1990; Longo, 2005). The emplacement of the Portachuela batholith began at ca. 24 Ma (Litherland et al., 1994), whereas volcanic activity in the Cajamarca district initiated at ca. 23 Ma (Fig. 1c; Longo, 2005; Chiaradia et al., 2009a). Late Miocene–Pliocene magmatism followed the Quechua II orogeny (12–11 Ma) during the subduction of the Inca Oceanic Plateau (Gutscher et al., 1999; Longo, 2005). The Quechua II orogeny was marked by the peak of crustal thickening and uplift in northern Peru (Noble et al., 1990; Sandeman et al., 1995; Chiaradia et al., 2009a; Michalak et al., 2016). It produced the Rio Blanco porphyry complex, Cordillera Blanca batholith, and an extensive volcanic flare-up in the Cajamarca

Fig. 1. (a) Topographic anomalies of the Nazca Plate and present-day position of the Inca Oceanic Plateau. (b) Position of the Inca Oceanic Plateau at 12–10 Ma, when the giant Rio Blanco and Yanacocha deposits formed (modified from Gutscher *et al.,* 1999; Chiaradia *et al.,* 2009a). (c) Simplified geological map of northern Peru (modified from Coba *et al.,* 2018). Abbreviations: HD = Huancabamba deflection.

district (Petford & Atherton, 1996; Davies, 2002; Longo, 2005; Giovanni, 2007; Margirier *et al.,* 2015). During this period, the convergence rate was reduced to ca. 11 cm/yr (Somoza, 1998; Somoza & Ghidella, 2012). The upper-crustal arc magmatism ceased during the flat-slab sub-duction of the Inca Oceanic Plateau (Gutscher *et al.,* 1999; Longo, 2005). Meanwhile, the magmatism slightly migrated eastward within the Cajamarca district (Longo,

2005; Longo *et al.,* 2010) and shifted southward until the youngest Cordillera Blanca batholith was emplaced at ca. 3 Ma (Fig. 1c; Petford & Atherton, 1996).

Miocene porphyry systems and igneous geochemistry in northern Peru

The Miocene metallogenic belt of northern Peru consists of many porphyry Cu systems formed at 25–8 Ma (Fig. 1c),

including porphyry Cu–Au–Mo deposits, such as the Minas Conga (23.2–15.6 Ma), Michiquillay (20.2–19.8 Ma), El Galeno (ca. 17.5 Ma), and the Yanacocha high-sulfidation epithermal Au deposit (12.3–8.4 Ma) in the Cajamarca district (Davies & Williams, 2005; Chiaradia et al., 2009a); the Cerro Corona porphyry Cu–Au deposit (ca. 13.4 Ma) and Tantahuatay epithermal Au deposit (ca. 12.4 Ma) in the Hualgayoc district (Macfarlane, 1999; Rosenbaum et al., 2005); the Lagunas Norte epithermal Au deposit (ca. 17 Ma) and La Arena porphyry Cu–Au deposit (ca. 25 Ma) in the Alto Chicama district (Montgomery, 2012); and the isolated La Granja porphyry Cu–Mo deposit (13.8–12 Ma) and Rio Blanco Cu–Mo deposit (ca. 11.2 Ma; Díaz et al., 1997; Chen et al., 2022).

Compared with Early–Middle Miocene porphyry Cu systems (25–16 Ma), those that formed during the Late Miocene (13–8 Ma) are coeval with the subduction of the Inca Oceanic Plateau and associated with adakitic magmatism (Davies, 2002; Chiaradia et al., 2009a). These adakitic magmas (cf. Richards & Kerrich, 2007) exhibit higher Sr/Y ratios (50–180), lower Y contents (4–13 ppm), and steeper fractionated rare earth element (REE) patterns at higher La_N/Yb_N ratios (14–26; Montgomery, 2012). Late Miocene igneous rocks related to mineralization display similar initial $^{87}Sr/^{86}Sr$ ratios (0.7043–0.7056) and initial $^{143}Nd/^{144}Nd$ ratios (0.51250–0.51276) to those associated with Neogene porphyry Cu deposits in central Chile (Reich et al., 2003; Stern et al., 2011; Loucks, 2021). Previous studies suggest that this relatively depleted isotopic characteristic is attributed to minor crustal contamination (Petford & Atherton, 1996; Davies, 2002).

Geology of Rio Blanco district

The exposed basement rocks in the Rio Blanco district are of the Paleozoic Salas Group and the Rio Seco Formation. Phyllites and metavolcanics of the Salas Group are conformably overlain by the metamorphosed quartzite of the Rio Seco Formation (Luis & Julio, 1987; Luis & Julio, 2017). These metamorphic basement rocks have not been intersected by drill holes.

The geology and geochronology of Rio Blanco are summarized as follows (Chen et al., 2022). The Miocene Portachuela batholith is the main host to the Rio Blanco porphyry complex (Figs 2 and 3) and was emplaced prior to the collision of the Inca Oceanic Plateau with the South American plate (12–10 Ma; Gutscher et al., 1999). The batholith is composed of tonalitic, dioritic, and granodioritic rocks. An igneous amphibole mineral separate from the batholithic sample was dated using the K–Ar radiometric method at 24 ± 5 Ma (Litherland et al., 1994), whereas igneous rock samples from the Rio Blanco district were dated at 14.48 ± 0.13 Ma (2σ) for tonalite and 12.43 ± 0.13 Ma (2σ) for quartz diorite (Table 2; Fig. 4; Chen et al., 2022). In comparison, the Rio Blanco porphyry complex consists mainly of granodioritic rocks (Figs 2 and 3). The porphyry complex consists of two intermineralization phases, namely

lower porphyry (11.45 ± 0.17 to 10.92 ± 0.14 Ma, 2σ) and upper porphyry (11.50 ± 0.17 Ma, 2σ), and four late-mineralization phases, namely one quartz–plagioclase porphyry (10.02 ± 0.12 to 9.91 ± 0.12 Ma, 2σ), two stages of porphyritic dacite dikes (10.62 ± 0.16 to 9.57 ± 0.13 Ma, 2σ; Table 2) in the orebody (Figs 2 and 3), and one quartz porphyry (9.06 ± 0.09 Ma, 2σ) located ca. 2.5 km to the northwest of the orebody (Chen et al., 2022). These previously published geochronological results suggest that the emplacement of the Rio Blanco porphyry complex postdates its hosted batholith (24–12 Ma) and is coeval with the subduction of the Inca Oceanic Plateau.

According to recent estimates, the Rio Blanco contains 1257 million metric tons of ore averaging 0.57 wt % Cu and 0.023 wt % Mo, with a cutoff grade of 0.4 wt % Cu (Monterrico Metals Ltd., internal report, 2006). Three magmatic–hydrothermal cycles have been identified at Rio Blanco (Fig. 4). The first (main) cycle was associated with intermineralization lower and upper porphyries and responsible for most of the ca. 99% hypogene Cu resources. This cycle progressively developed potassic (biotite ± K–feldspar), propylitic (chlorite–epidote), sericite–chlorite, and quartz–sericite alterations (Fig. 2). Relics of potassic alteration (mainly biotite) can be observed in the western, eastern, and southern parts of the orebody. The central part of the orebody is dominated by sericite–chlorite and quartz–sericite alterations, which were cut by quartz–sericite-cemented breccia. Most of the first-cycle mineralization occurred as dissemination and D-type veins in the sericite–chlorite and quartz–sericite alteration zones, and as cement filling in the breccia. The propylitic alteration that developed in the periphery of the orebody generally has no economic or subeconomic Cu–Mo grade. A molybdenite sample from a D-type vein yielded a Re–Os model age of 11.43 ± 0.16 Ma (Chen et al., 2022). Two molybdenite separate samples from the quartz–sericite-cemented breccia have model ages of 11.28 ± 0.24 and 11.11 ± 0.18 Ma (2σ; Chen et al., 2022). Additionally, a sample of hydrothermal sericite separate from the first-cycle alteration zone yielded a K–Ar age of 11.2 ± 0.5 Ma (Bristow & Pratt, 2005). These ages also indicate that the main mineralization (first cycle) was related to the lower and upper porphyries.

The second magmatic–hydrothermal cycle was associated with late-mineralization porphyritic dacite 1 (Fig. 4), which caused biotite alteration in the eastern part of the orebody and biotite–anhydrite-cemented breccia in tonalite (Fig. 2). Mineralization in this cycle consisted mainly of disseminated chalcopyrite in the biotite alteration zone and formed cement in the breccia. The second cycle was responsible for the remaining 1% of the economic hypogene Cu resource. A hydrothermal biotite separate sample that crystallized during this cycle yielded a K–Ar age of 10.4 ± 0.4 Ma (Bristow & Pratt, 2005).

The third magmatic–hydrothermal cycle was associated with late-mineralization quartz–plagioclase porphyry, porphyritic dacite 2, and quartz porphyry (Fig. 4),
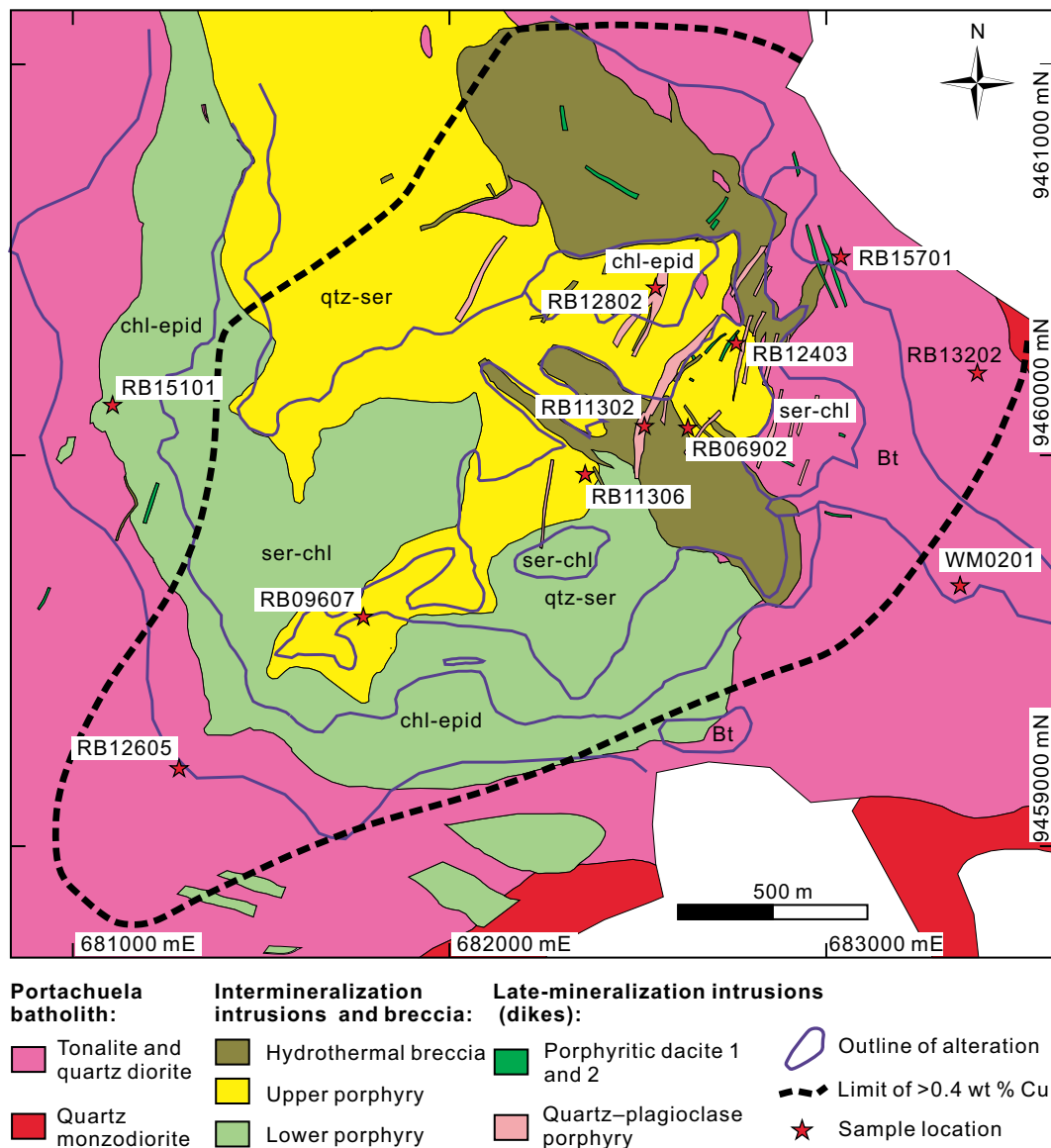
Fig. 2. Simplified geologic map of the Rio Blanco deposit (based on Chen *et al.,* 2022). Coordinate system: PSAD 1956 UTM Zone 17 S. Abbreviations: Bt, biotite; chl-epid, chlorite–epidote; qtz-ser, quartz–sericite; ser-chl, sericite–chlorite.

leading to the development of propylitic, sericite–chlorite, and sericite alteration assemblages in discrete intrusions that are not of economic interest. Most of the sulfide mineralization consists of disseminations hosted in the altered rocks.

ANALYTICAL METHODS
Sample preparation and selection

The least-altered samples from the Portachuela batholith and Rio Blanco porphyry complex were collected from drill cores for whole-rock major-element, trace-element, and Sr–Nd isotope analyses. Fresh amphibole, biotite, plagioclase, and apatite minerals were selected for electron probe microanalysis (EPMA). Zircon grains were separated and mounted in epoxy resin for Hf–O isotope and trace-element analyses. The whole-rock

major and trace elements, whole-rock Sr–Nd isotopic values, and zircon Hf–O isotopic values were employed to investigate the origin and evolution of the magmas. Mineral compositions were used to constrain the magmatic crystallization conditions and volatile composition (temperature, pressure, oxygen fugacity, H_2O content, and S content). Sample descriptions and locations are provided in Table 1.

Most of the amphibole grains (Fig. 5a and b) in the batholith samples are subhedral and have two sets of cleavage planes with grain sizes of 0.1–2.0 mm. With regard to the porphyry complex, although there are some mafic minerals with the crystal habit of amphibole, most samples are altered, so they could not be analyzed. No amphibole is observed in the least-altered samples of lower porphyry (RB15101) and porphyritic dacite 1 dike (RB15701; Table 1).
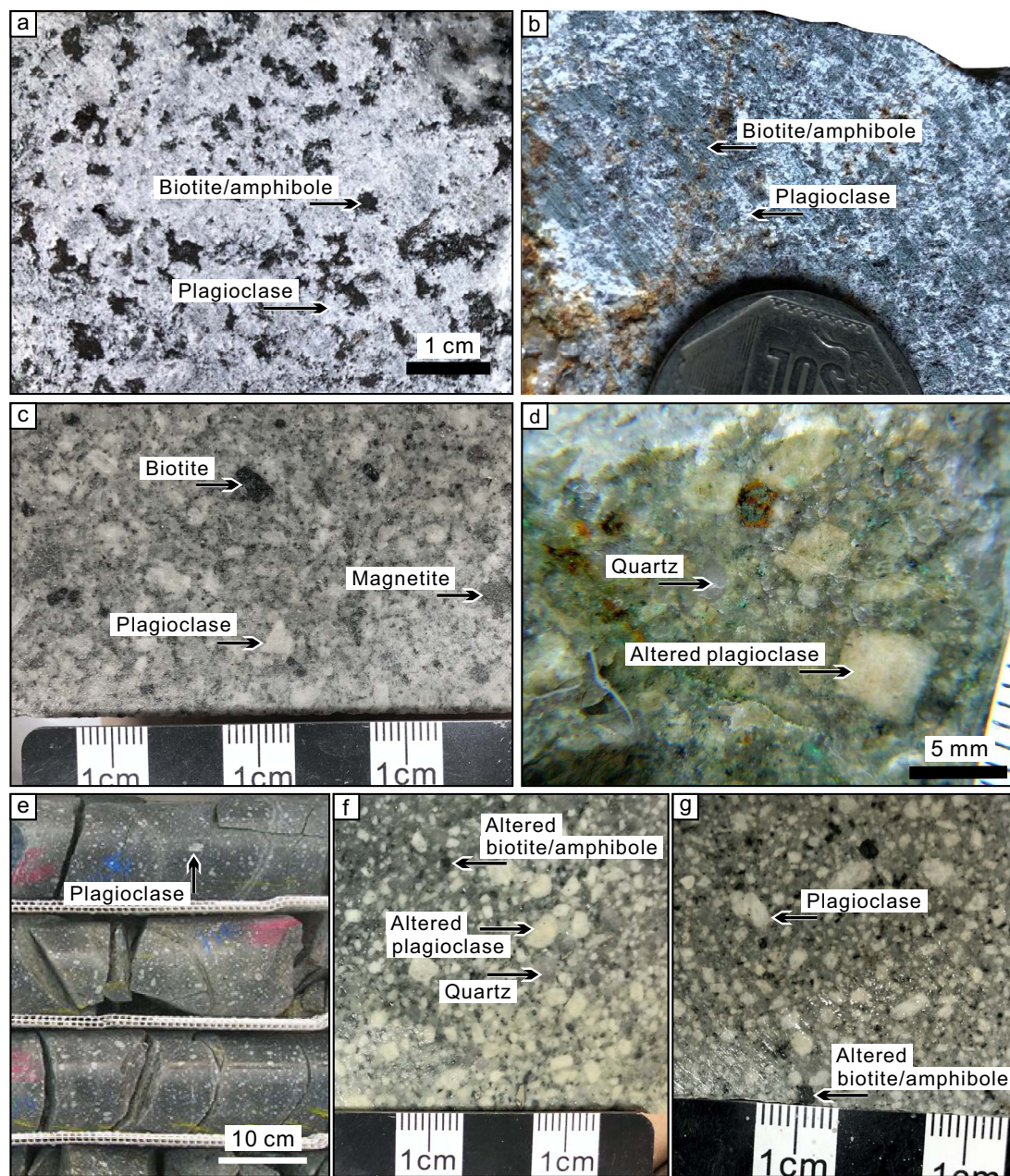
Fig. 3. Hand specimen photographs of the Portachuela batholith and Rio Blanco porphyry complex. (a) Portachuela batholith tonalite. (b) Portachuela batholith quartz diorite. (c) Intermineralization lower porphyry, which has crowded plagioclase phenocrysts with a weak chlorite–sericite alteration. (d) Intermineralization upper porphyry with sporadic plagioclase and quartz phenocrysts (photo from Chen *et al.*, 2022). (e) Late-mineralization porphyritic dacite 1, with uniformly distributed hydrothermal biotite giving the rock a dark overall color. (f) Late-mineralization quartz–plagioclase porphyry with a moderate chlorite–sericite alteration. (g) Late-mineralization porphyritic dacite 2 with a moderate chlorite–sericite alteration.

The subhedral igneous biotite grains in the batholith samples, with sizes of 0.1–5.0 mm, are generally intergrown with amphibole. The lower porphyry (RB15101) and porphyritic dacite 1 (RB15701) have igneous biotite phenocrysts that are subhedral to euhedral and have grain sizes of 0.1–6.0 mm (Fig. 5).

The plagioclase grains in the batholith samples, with sizes of 0.1–10.0 mm, are fresh and anhedral to subhedral. The plagioclase phenocrysts in the lower porphyry (RB15101) and porphyritic dacite 1 (RB15701) are generally fresh and euhedral, with grain sizes of 1–5 mm.

In particular, the phenocrysts in the lower porphyry (RB15101) exhibit compositional zoning (Fig. 6), which is locally observed in porphyritic dacite 1 (RB15701). Apatite crystals are commonly observed within the plagioclase grains in the batholith and porphyry samples (Fig. 6a–c), whereas zircon crystals are rarely observed (only eight grains were found) to occur in the rims of the plagioclase grains (seven of the eight grains; Fig. 6f and g).

The apatite inclusions in fresh plagioclase (Fig. 6a–c), amphibole, and biotite are generally euhedral and are 5–100 and 1–20 μm in length and width, respectively
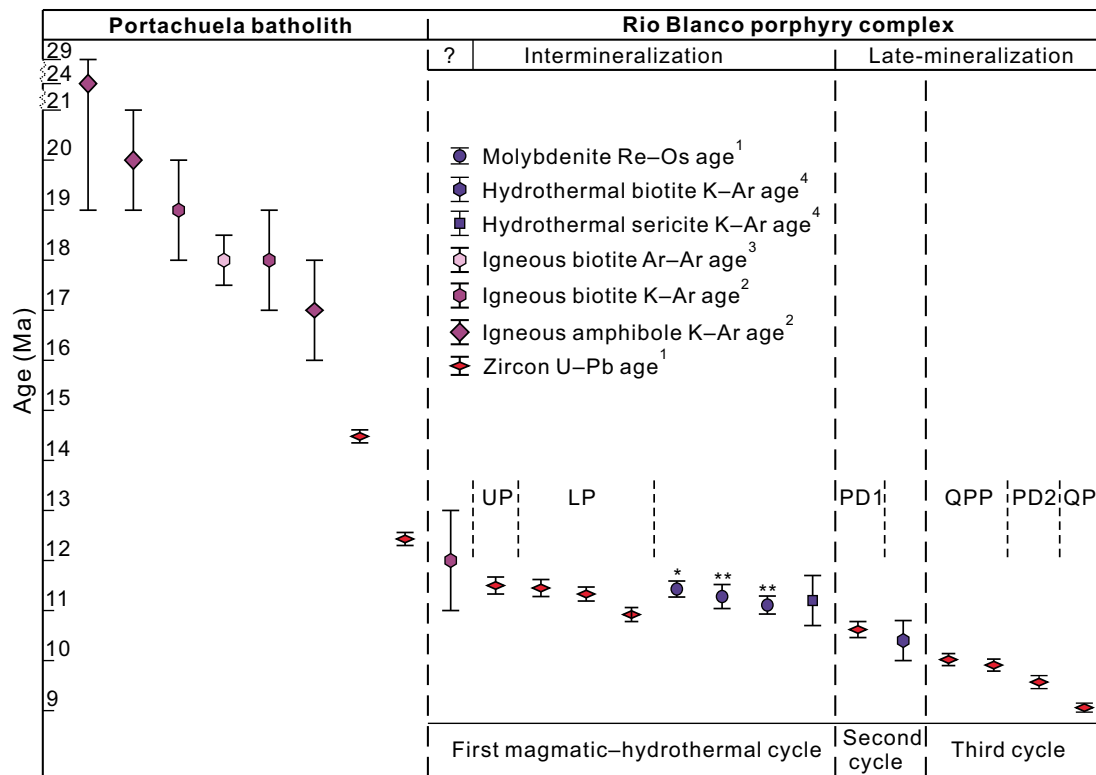
Fig. 4. Summary of radiometric ages of the Portachuela batholith and Rio Blanco porphyry complex. Sources: [1]Chen *et al.* (2022); [2]Litherland *et al.* (1994); [3]Urlich (2005); [4]Bristow & Pratt (2005). Sample locations: ∗, molybdenite-bearing D-type vein; ∗∗, hydrothermal breccia cemented by quartz and sericite. Abbreviations: LP, lower porphyry; PD1, porphyritic dacite 1; PD2, porphyritic dacite 2; QPP, quartz–plagioclase porphyry; QP, quartz porphyry; UP, upper porphyry.

(Fig. 6). Apatite grains that are in groundmass, close to microfractures, or intergrown with hydrothermal sericite and sulfide, had probably been altered (Cao *et al.,* 2021; Fig. 6d and e). Thus, we instead analyzed the apatite inclusions in the fresh plagioclase grains to constrain the original composition.

Whole-rock analyses

Major- and trace-element analyses were conducted at Wuhan Sample Solution Analytical Technology Co., Ltd., Hubei, China. The rocks were crushed and powdered to less than 200 mesh. The powdered samples (100 g for each) were placed in an oven at 105°C for drying for 12 h. The detailed procedure of sample digestion for the major-element analyses was described by Wang *et al.* (2020). The major elements were analyzed via X-ray fluorescence (Primus II, Rigaku, Japan) using a Rh-anode X-ray tube with a voltage of 50 kV and current of 60 mA. The calibration curves used for quantification were produced through bivariate regression of data from about 43 reference materials encompassing a wide range of silicate compositions. The analytical precision for major oxides, based on certified standards (GSR–1 and GSR–3) and duplicate analyses, were generally less than 5%. Ferrous iron measurements were performed via wet chemical analyses (titration). Whole-rock trace-element analyses were conducted using an Agilent 7700e induc-

tively coupled plasma mass spectrometer (ICP–MS). The analytical precision of the trace-element contents was better than 5%.

Whole-rock Sr–Nd isotopic analyses were performed on a Neptune Plus multicollector ICP–MS at Wuhan Sample Solution Analytical Technology Co., Ltd. The Sr and Nd mass fractionations were corrected by $^{88}Sr/^{86}Sr = 8.375209$ and $^{146}Nd/^{144}Nd = 0.7219$, respectively (Lin *et al.,* 2016). NIST SRM 987 analyses and the Alfa Sr standard solution yielded $^{87}Sr/^{86}Sr$ ratios of 0.710241 ± 0.000004 (2SD, $n = 6$) and 0.708708 ± 0.000004 (2SD, $n = 6$), respectively. These values were identical within uncertainty to the standard values (0.710241 ± 0.000012) of the reference material NIST SRM 987 reported in Thirlwall (1991) and to long-term Alfa Sr values of 0.708717 ± 0.000012. Analyses of the GSB and Alfa Nd reference materials yielded $^{143}Nd/^{144}Nd$ ratios of 0.512442 ± 0.00006 (2SD, $n = 9$) and 0.512444 ± 0.00006 (2SD, $n = 9$), respectively. The results were in agreement within uncertainty to the recommended value for GSB (0.512439 ± 0.00001; Li *et al.,* 2017) and long-term in-house Alfa Sr data of 0.512446 ± 0.000007. In addition, BCR-2 and AGV-2 monitor materials yielded results of 0.705008 ± 0.000008 (2SD, $n = 1$) and 0.703975 ± 0.000007 (2SD, n = 1) for $^{87}Sr/^{86}Sr$ and 0.512636 ± 0.000004 (2SD, $n = 1$) and 0.512789 ± 0.000004 (2SD, $n = 1$) for $^{143}Nd/^{144}Nd$, respectively. These were within the errors of their recommended values (Zhang & Hu, 2020).

Table 1: Sample description of Portachuela batholith and Rio Blanco porphyry

Sample	Location X (m)	Y (m)	Z (m)	Unit	Rock type	Description	Whole-rock major- and trace-element	Whole-rock Sr-Nd	Zrn Hf-O	Mineral composition Zrn[1]	Amp[2]	Bt[2]	Pl[2]	Ap[2]
WM0201	683358	9459654	2071	Batholith	To	Equigranular. Unaltered. Pl (~55%), Kf (~10%), Qtz (~20%), Bt (~10%), Amp (1-5%).	×	×	×	×	×	×	×	×
RB13202	683414	9460223	1935		To	Equigranular. Unaltered. Pl (~55%), Qtz (~20%), Bt (~10%), Kf (~10%), Amp (1-5%).	×	×			×	×	×	×
RB12605	681267	9459156	2432		Q-d	Slight alteration. Pl and MM are fresh. Pl (50-55%), Kf (10-15%), Qtz (~10%), Bt (10-15%), Amp (1-5%).	×				×	×	×	
RB15101	681095	9460140	2309	Intermineralization	LP	Porphyritic. Unaltered. Crowded phenocryst (50-80%): Pl (~60%) and Bt (~10%) are fresh; Qtz (~5%). Mt (~5%); no Amp was observed.	×	×				×	×	×
RB09607	681783	9459580	2496		LP	Porphyritic. Slight alteration. Crowded to sparse phenocryst (~75%): Pl (~60%) part altered; no fresh Bt (~10%); Qtz (~5%).	×	×	×	×	×		×	
RB12403	682785	9460306	1941		LP	Porphyritic. Strong alteration and texture destructed.	×		×	×				
RB15701	683042	9460536	2076	Late-mineralization	PD1	Porphyritic. Slight alteration. Sparse phenocryst (~15%): Pl (~10%) and Bt (~2%) are frash; Qtz (~2%); no Amp was observed.	×		×	×		×	×	×
RB12802	682540	9460443	2042		QPP	Porphyritic. Strong alteration and texture partly destructed.	×		×	×				
RB11302	682526	9460084	2285		QPP	Porphyritic. Moderate alteration. Sparse phenocryst (~45%): Pl (5-20%) part altered; Qtz (5-20%); no fresh MM (~5%) mineral.	×							
RB06902	682668	9460076	2320		PD2	Porphyritic. Moderate alteration; Sparse phenocryst (~10%): Pl (~5%) part altered; Qtz (~2%); no fresh MM (~3%) mineral.	×	×					×	×
RB11306	682371	9459958	1992		PD2	Sparse phenocryst (~10%), Pl (~5%) part altered; Qtz (~2%); no fresh MM (~3%) mineral.	×							

Coordinate system: PSAD 1956 UTM Zone 17 S. Abbreviation: Amp = amphibole; Ap = apatite; Bt = biotite; Kf = K-feldspar; LP = lower porphyry; MM = mafic mineral (biotite and amphibole); Mt = magnetite; PD1 = porphyritic dacite 1; PD2 = porphyritic dacite 2; Pl = plagioclase; Q-d = quartz diorite; QPP = quartz-plagioclase porphyry; Qtz = quartz; To = tonalite; UP = upper porphyry; Zrn = zircon; × = analyzed sample. [1]LA-ICP-MS (laser ablation–inductively coupled plasma-mass spectrometry). [2]EPMA.

Table 2: Summary of radiometric ages of Portachuela batholith and Rio Blanco porphyry complex

Intrusive unit	lithology	Sample	Age (Ma)
Portachuela batholith	Hornblende-biotite granodiorites and diorites	CCR87/27C (Hb)[1]	20 ± 1
		CCR87/27C (Bt)[1]	17 ± 1
		CCR87/27F (Hb)[1]	24 ± 5
		CCR87/27F (Bt)[1]	19 ± 1
		CCR87/27G (Bt)[1]	18 ± 1
		GA-019 (Hb)[2]	18 ± 0.5
	Tonalite	WM-02-01 (Zrn)[3]	14.48 ± 0.13
	Quartz diorite	RB-126-05 (Zrn)[3]	12.43 ± 0.13
Porphyry complex	Biotitic felsic porphyry	CCR87/27A (Bt)[1]	12 ± 1
		RB-137-02 (Zrn)[3]	11.45 ± 0.17
	Intermineralization lower porphyry	RB-096-07 (Zrn)[3]	11.33 ± 0.14
		RB-124-03 (Zrn)[3]	10.92 ± 0.14
	Intermineralization upper porphyry	RB-112-09 (Zrn)[3]	11.50 ± 0.17
	Late-mineralization porphyritic dacite 1	RB-157-01 (Zrn)[3]	10.62 ± 0.16
	Late-mineralization quartz–plagioclase porphyry	RB-113-02 (Zrn)[3]	10.02 ± 0.12
		RB-128-02 (Zrn)[3]	9.91 ± 0.12
	Late-mineralization porphyritic dacite 2	RB-069-02 (Zrn)[3]	9.57 ± 0.13
	Late-mineralization quartz porphyry	SH-002-02 (Zrn)[3]	9.06 ± 0.09

Analytical method: (Bt)[1] = biotite K–Ar; (Hb)[1] = hornblende K–Ar; (Hb)[2] = hornblende Ar–Ar; (Zrn)[3] = zircon U–Pb. [1]Litherland *et al.* (1994). [2]Urlich (2005).. [3]Chen *et al.* (2022). [1] and [2] from approximately 20 km to the north of Rio Blanco, in Ecuador side.

Zircon Hf–O isotopes

Zircon Lu–Hf isotopes were measured at the Institute of Mineral Resources, Chinese Academy of Geological Sciences (CAGS), Beijing, China, using a NewWave UP213 laser ablation system coupled with a Neptune multi-collector ICP–MS. Laser ablation was carried out with a repetition rate of 6 Hz, a fluence of 10 J/cm^2, and a beam diameter of 55 μm. Helium gas was used as a carrier gas in combination with Ar to transport the ablated aerosol from the laser ablation cell to the ICP–MS torch via a mixing chamber. $^{176}Lu/^{175}Lu$ and $^{176}Yb/^{173}Yb$ ratios were determined (0.02658 and 0.796218, respectively; Chu *et al.,* 2002) to correct the isobaric interferences of ^{176}Lu and ^{176}Yb on ^{176}Hf. For instrumental mass bias correction, Yb isotope ratios were normalized to a $^{172}Yb/^{173}Yb$ ratio of 1.35274, and Hf isotope ratios to a $^{179}Hf/^{177}Hf$ ratio of 0.7325, using exponential correction. The mass bias behavior of Lu was assumed to follow that of Yb; the mass bias correction protocol was described by Wu *et al.* (2006) and Hou (2007). Zircon GJ-1 was used as the reference standard during our routine analyses, which yielded a weighted mean $^{176}Hf/^{177}Hf$ ratio of 0.281990 ± 0.000010 (2σ, n = 18). The value is indistinguishable from the weighted mean $^{176}Hf/^{177}Hf$ ratio of 0.282000 ± 0.000005 (2σ), which was obtained by Morel *et al.* (2008) using solution analysis. The initial $^{176}Lu/^{177}Hf$ ratios were calculated using a decay constant of 1.867 × 10^{-11} yr^{-1} for ^{176}Lu (Söderlund *et al.,* 2004). The chondritic $^{176}Lu/^{177}Hf$ ratio of 0.0332 and the $^{176}Hf/^{177}Hf$ ratio of 0.282772 (Blichert-Toft & Albarède, 1997) were adopted to calculate $\varepsilon_{Hf}(t)$ values.

Zircon oxygen isotopes were measured using a Cameca IMS 1280-HR ion microprobe at the Beijing Research Institute of Uranium Geology, Beijing, China. The detailed analytical procedures and instrumental parameters were described by Li *et al.* (2010a). A $^{133}Cs^+$ primary beam was focused on a 20-μm-diameter spot for the zircon analyses. The measured oxygen isotopic data were first normalized relative to the Vienna Standard Mean Ocean Water (VSMOW), with $(^{18}O/^{16}O)_{VSMOW} = 0.0020052$ (Baertschi, 1976). The instrumental mass fractionation factor was corrected using a Penglai primary reference material with a $\delta^{18}O_{VSMOW}$ value of 5.31 ± 0.10‰ (Li *et al.,* 2010b). The $\delta^{18}O$ value of the monitor Qinghu was 5.54 ± 0.06‰ (2σ, n = 21), consistent with the recommended value of 5.4 ± 0.2‰ (Li *et al.,* 2013).

Electron probe microanalysis

Compositional analyses of hornblende, plagioclase, biotite, and apatite in polished thin sections were conducted using an electron microprobe (JEOL JXA-8230 Superprobe) at the Wuhan Sample Solution Analytical Technology Co., Ltd. The operating conditions were as follows: an accelerating voltage of 15 kV, a beam current of 20 nA, and a beam diameter of 3 μm (hornblende, plagioclase, and biotite). ZAF correction was used for data reduction. For microcrystalline apatite of <3 μm width, we used a small beam size of 1 μm. We analyzed F and Cl using a short analysis time (10 s) to minimize potential decomposition by beam damage. The analyzed elements, analyzing crystals, times of peaks and backgrounds,
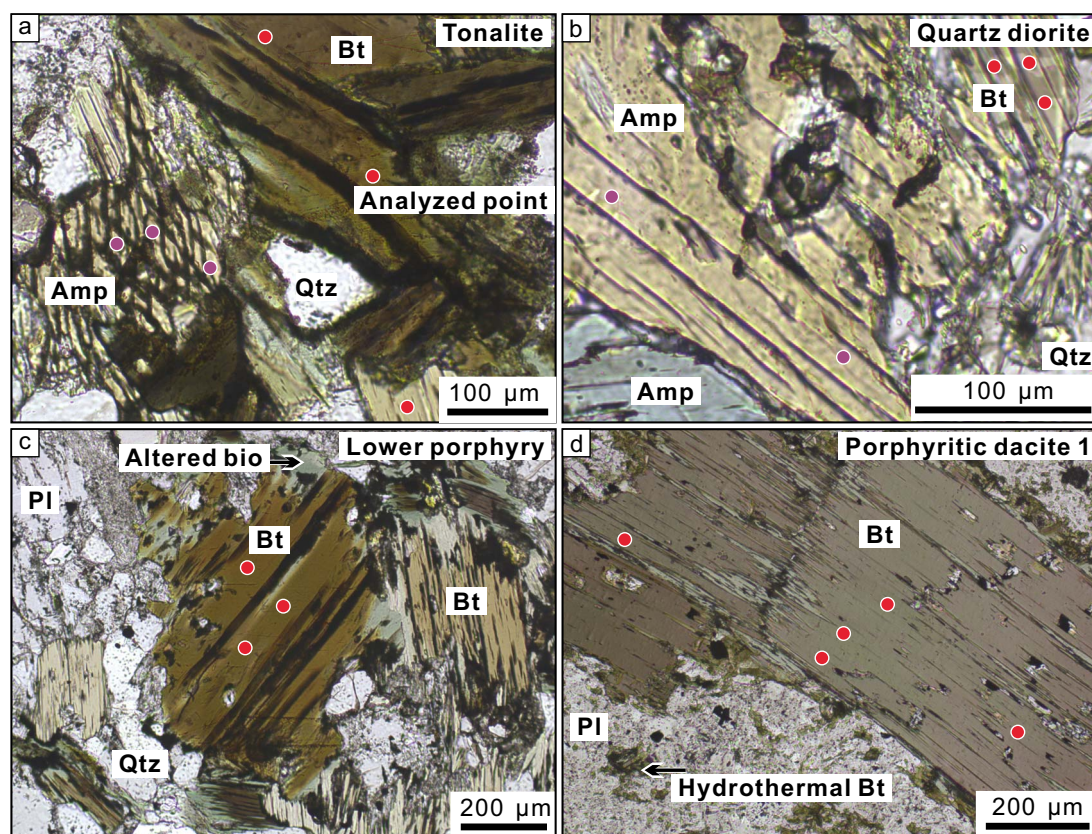
Fig. 5. Photomicrographs (plane polarized transmitted light) of amphiboles and biotites in samples from (a) tonalite, (b) quartz diorite, (c) lower porphyry, and (d) porphyritic dacite 1. Abbreviations: Amp, amphibole; Bt, biotite; Pl, plagioclase; Qtz, quartz.

standards, and detection limits are provided in Electronic Appendix Table A1.

To test the reliability of the electron probe analyses of apatite S, Cl, and F concentrations using small beam sizes (1 and 3 μm), we performed apatite analyses using beam sizes of 5, 3, and 1 μm in adjacent areas of a standard Durango apatite and in apatite grains from tonalite and porphyritic dacite 2 of the Rio Blanco intrusion (Electronic Appendix B). Considering apatite decomposition can be minimized using a 5-μm beam size (Xu et al., 2021; Meng et al., 2021a), we compared the results obtained using the 5-μm beam with those obtained using the 3- and 1-μm beams. We assumed that the relative difference was mainly caused by apatite decomposition vs intra-grain heterogeneity because each series of analytical spots (for the three beam sizes) were adjacent and in the same apatite chemical zoning (Electronic Appendix B). The results suggested that most of the relative differences in apatite S content (5 vs 3 μm, and 5 vs 1 μm) were <15% (Fig. A2), whereas those in apatite Cl content were <10% (Fig. A3). The standard Durango apatite had large relative differences in S and Cl contents of <23% and <27%, respectively (Figs A2 and A3). The relative differences in apatite F content were high, up to 77%, suggesting a strong effect of apatite decomposition on F analyses. Hence, we excluded the F concentration results from the interpretation and discussion.

Zircon trace-element analyses

Trace elements in zircon were measured at the Institute of Mineral Resources, CAGS. Laser sampling was performed using a UP213 laser ablation system, and a Thermo Finnigan Neptune ICP–MS was used to measure the trace-element abundances. Cathodoluminescence, transmission, and reflection images were used to select clear (inclusion-free) zircon crystals with oscillatory/ sector zoning. The laser parameters were as follows: repetition rate of 5 Hz, fluence of 6 J/cm^2, and spot diameter of 38 μm. NIST SRM 610 and 91 500 were used as primary and secondary reference materials, respectively, with Si as an internal standard. The results for the secondary reference materials agreed within uncertainty ($\pm$ 10%) with previously published values.

RESULTS
Whole-rock geochemistry

The major- and trace-element abundances for eight samples of intrusive rocks are shown in Table 3 and Figs 7 and 8. All of the analyzed rock samples fall within the dioritic–granodioritic fields defined by Le Bas et al. (1986). The batholith and porphyry complex rock samples are calc-alkaline except one late-mineralization sample of high-K calc-alkaline quartz–plagioclase porphyry,
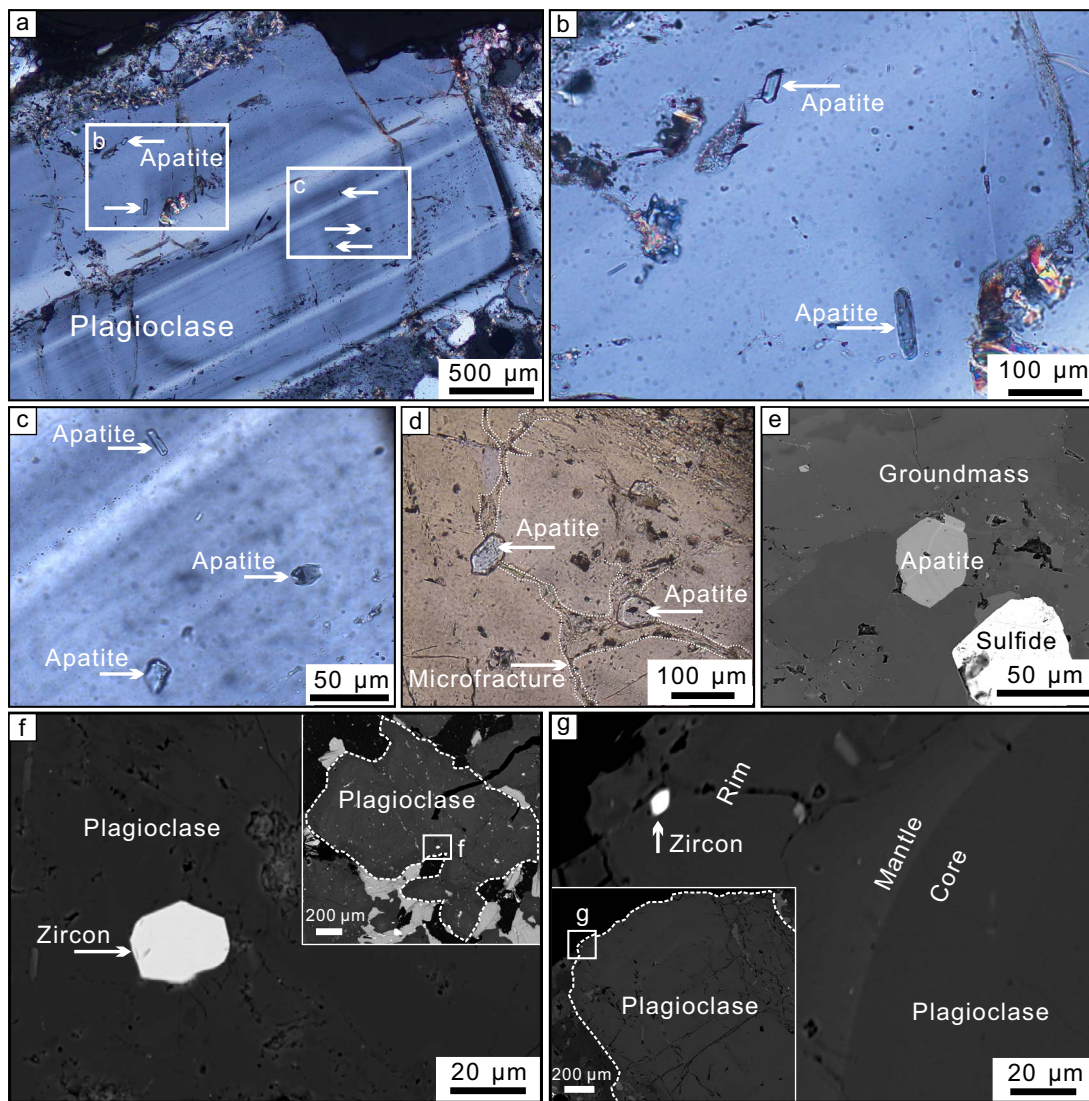
Fig. 6. (a–c) Igneous apatite crystals in the unaltered plagioclase phenocrysts of the intermineralization lower porphyry. (d) Apatite grains in plagioclase, close to a microfracture in quartz diorite. (e) Apatite in groundmass, close to hydrothermal sulfide minerals (pyrite and chalcopyrite). (f) Backscattered electron (BSE) image showing a zircon trapped in the rim of a plagioclase grain of the tonalite sample. (g) BSE image showing a zircon trapped in the rim of a plagioclase grain of the lower porphyry sample.

which may have been altered, considering the high loss on ignition (LOI) value of 4.32 wt % (Table 1; Fig. 7b). All samples are slightly peraluminous, with ASI (molar $Al_2O_3/(CaO + Na_2O + K_2O)$ ratio) values of 1.0–1.2 (Table 3). These samples show strong enrichment in large-ion lithophile elements (LILEs; e.g. Rb, Ba, Th, and K), depletion of high-field-strength elements (HFSEs; e.g. Nb and Ta), and a negative Ti anomaly (Fig. 8a). No significant Eu anomalies ($Eu_N/(0.5 \times (Sm_N + Gd_N)) = 0.9$–1.2; average at 1.02) are detected. All of the igneous rocks exhibit adakitic geochemical signatures (Fig. 9a; e.g. $SiO_2 \geq 56$ wt %, $Al_2O_3 \geq 15$ wt %, Sr/Y ≥ 20; cf. Richards & Kerrich, 2007). However, compared with the rocks of the Portachuela batholith, those of the porphyry complex have steeper REE patterns (Fig. 8b) and higher Sr/Y ratios (45.9–55.4 vs 85.3–174.9), La_N/Yb_N ratios (8.5–9.6 vs 14.7–26.2), and Dy/Yb ratios (1.95–2.04 vs 1.88–2.26). These differences have been observed in other Miocene igneous

rocks in northern Peru dated between 23–12 and 12–8 Ma (Figs 8 and 9).

Zircon Hf–O and whole-rock Sr–Nd isotopic compositions

The ranges in zircon Hf–O isotopic composition are remarkably uniform between various intrusive units, and the isotopic values show no correlation with the U–Pb age and whole-rock SiO_2 content (Fig. 10). These samples have comparable zircon $\varepsilon_{Hf}(t)$ values of -2.1 to $+3.2$ (0.3 ± 1.2 on average, SD, $n = 86$) and indistinguishable narrow ranges of zircon $\delta^{18}O$ values of 6.23‰–6.85‰ ($6.5 \pm 0.14‰$ on average, SD, $n = 86$).

Intrusive rocks in Rio Blanco also have uniform Sr–Nd isotope values, with initial $^{87}Sr/^{86}Sr$ values ranging from 0.70468 to 0.70483 and initial $^{143}Nd/^{144}Nd$ values ranging from 0.51260 to 0.51261 ($\varepsilon_{Nd} = -0.5$ to -0.3). These results are similar to those of the Miocene igneous rocks in

Table 3: Whole-rock element and isotopic compositions of Rio Blanco intrusions

Unit	Batholith		Intermineralization		Late mineralization			
Lithology	Tonalite		Lower porphyry		PD1	QPP	PD2	
Sample	WM0201	RB13202	RB9607	RB15101	RB15701	RB11302	RB6902	RB11306
SiO_2 (wt %)	61.31	61.24	66.70	65.76	65.44	66.65	67.74	68.07
TiO_2	0.70	0.72	0.51	0.55	0.50	0.33	0.37	0.36
Al_2O_3	17.90	17.59	16.83	17.27	16.97	15.81	16.40	16.60
Fe_2O_3(total)	5.30	5.94	3.38	3.70	3.25	2.05	2.72	2.02
FeO	2.88	3.10	2.20	1.84	2.32	1.08	1.70	1.22
MnO	0.08	0.08	0.04	0.06	0.04	0.07	0.13	0.04
MgO	2.66	2.72	1.53	1.36	1.59	1.05	1.04	1.08
CaO	5.19	5.47	3.30	3.78	3.65	3.29	2.59	3.45
Na_2O	3.99	3.68	4.25	4.45	4.76	2.61	4.30	4.47
K_2O	1.71	1.42	1.14	1.73	1.34	3.15	2.17	2.08
P_2O_5	0.16	0.17	0.16	0.15	0.16	0.12	0.13	0.13
LOI	0.55	0.96	1.54	1.13	0.99	4.32	1.27	1.57
Total	99.54	99.99	99.38	99.95	98.68	99.45	98.86	99.86
Cs (ppm)	4.51	2.28	1.75	8.41	3.37	6.85	2.47	2.31
Rb	69.11	58.64	36.74	49.23	85.56	138.77	66.14	80.79
Ba	478.82	481.49	483.75	573.75	361.95	803.98	883.12	702.67
Th	5.88	5.06	2.95	4.53	2.93	4.03	3.70	3.18
U	1.51	1.57	0.83	1.19	1.87	2.45	1.55	1.23
Nb	5.19	4.74	4.58	4.04	3.05	3.40	3.40	3.15
Ta	0.45	0.39	0.37	0.39	0.23	0.31	0.28	0.23
La	12.82	14.89	15.70	10.61	13.70	11.86	13.95	13.77
Ce	25.37	29.90	30.65	20.57	27.30	22.58	27.21	27.61
Pb	6.23	6.77	8.60	7.59	9.03	9.82	17.80	14.48
Pr	3.27	4.03	3.93	2.64	3.54	3.00	3.49	3.16
Sr	557.56	559.72	695.77	648.16	842.98	478.35	751.68	745.96
Nd	13.69	16.39	15.04	10.39	14.60	11.51	13.53	12.16
Sm	2.66	3.24	2.76	1.96	2.64	2.02	2.50	2.00
Zr	76.64	92.94	78.18	78.32	93.18	76.08	79.00	81.46
Hf	2.44	2.59	2.45	2.42	2.69	2.33	2.37	2.32
Eu	0.88	0.92	0.77	0.74	0.71	0.60	0.72	0.61
Gd	2.22	2.87	2.04	1.56	1.97	1.42	1.75	1.27
Tb	0.36	0.44	0.28	0.21	0.23	0.19	0.23	0.15
Dy	1.85	2.31	1.47	1.01	1.06	1.00	1.09	0.80
Ho	0.33	0.42	0.25	0.18	0.18	0.19	0.19	0.14
Y	10.07	12.20	7.65	5.09	5.50	5.61	5.85	4.27
Er	0.96	1.20	0.76	0.52	0.52	0.57	0.54	0.37
Tm	0.14	0.17	0.11	0.07	0.08	0.08	0.07	0.05
Yb	0.90	1.18	0.68	0.49	0.47	0.53	0.51	0.35
Lu	0.14	0.18	0.11	0.07	0.08	0.08	0.07	0.05
ASI	1.00	1.00	1.18	1.07	1.06	1.15	1.16	1.04
Sr/Y	55.36	45.88	90.90	127.25	153.17	85.32	128.45	174.87
La/Yb	14.18	12.57	23.10	21.74	29.29	22.18	27.26	38.82
Dy/Yb	2.04	1.95	2.16	2.08	2.26	1.88	2.12	2.26
La_N/Yb_N	9.56	8.48	15.57	14.66	19.74	14.96	18.38	26.17
Initial $^{87}Sr/^{86}Sr$	0.70483	0.70480	0.70477	0.70468			0.70479	
Initial $^{143}Nd/^{144}Nd$	0.51260	0.51261	0.51258	0.51260			0.51254	
AST (°C)	865	870		855	876			868

Initial $^{87}Sr/^{86}Sr$ and $^{143}Nd/^{144}Nd$ values are corrected to 11 Ma. Abbreviations: PD1, porphyritic dacite 1; PD2, porphyritic dacite 2; QPP, quartz–plagioclase porphyry.

northern Peru (Fig. 11). Samples RB9607 and RB6902 are outliers that may be due to the alteration (Table 1).

Mineral compositions and crystallization conditions
Amphibole
All of the analyzed amphibole grains from the batholith samples have low Al_2O_3 contents (2.4 wt %–7.8 wt %; Electronic Appendix Table A4). These amphibole grains are rich in magnesium, with Mg# (molar Mg/(Mg + Fe_{total})) varying from 0.62 to 0.79 and Al# (Al^{VI}/Al^T) ranging from 0.01 to 0.20. The thermodynamic formulas of Ridolfi (2021) were employed as the amphibole thermometer, hygrometer, and oxybarometer. Based on the reliability criteria for amphibole composition (Ridolfi, 2021), 20 of the 42 amphibole analysis results for tonalite, and
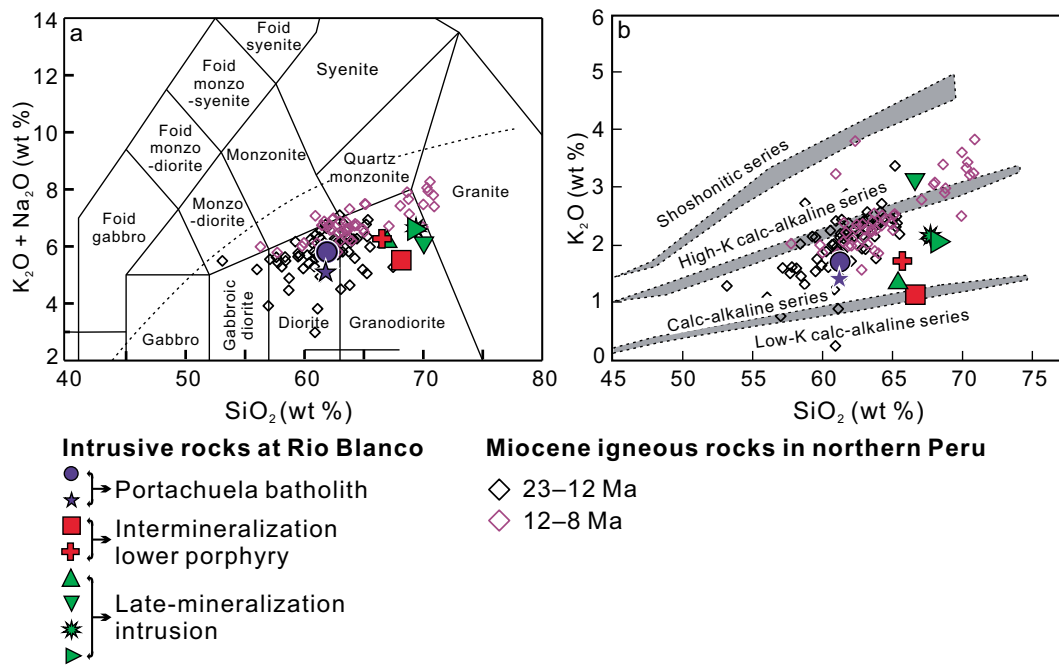
Fig. 7. (a) Diagram of Na$_2$O + K$_2$O vs SiO$_2$ (Le Bas *et al.*, 1986). (b) Diagram of K$_2$O vs SiO$_2$ (Rollinson, 2014). Miocene igneous rocks in northern Peru (data from Petford & Atherton, 1996; Macfarlane, 1999; Davies, 2002; Longo, 2005; Chiaradia *et al.*, 2009a; Montgomery, 2012; Mamani *et al.*, 2016; referring criteria of Loucks, 2014; LOI value <3.5 wt % or volatile-free total of 97.5 wt %–101.5 wt %).
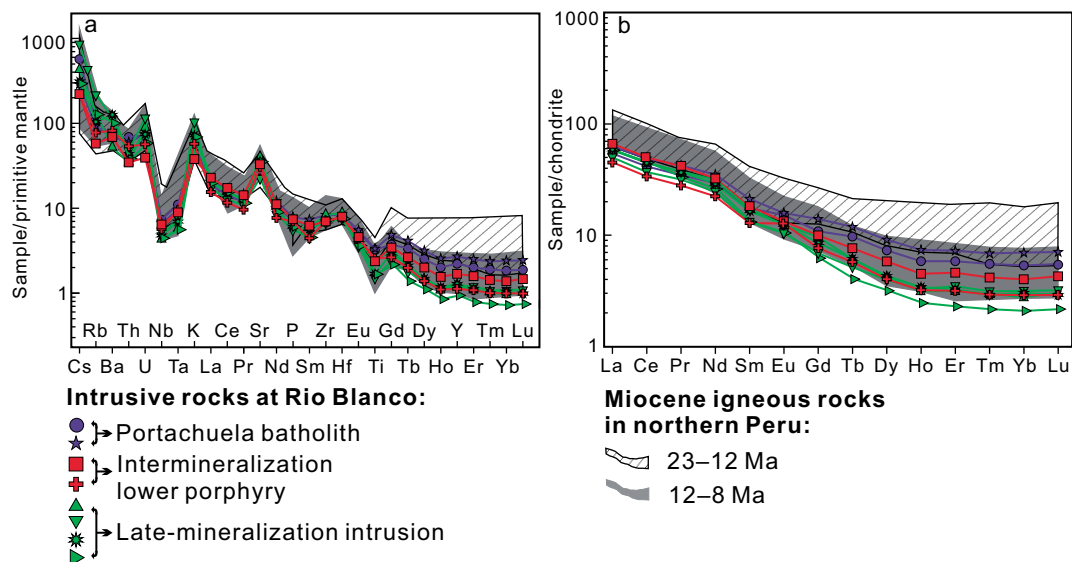

Fig. 8. (a) Primitive mantle-normalized trace-element patterns for Rio Blanco rocks. (b) Chondrite-normalized REE patterns for Rio Blanco rocks. The data on Miocene igneous rocks in northern Peru are from the literature. The primitive mantle and chondrite values are from Sun & McDonough (1989).

all of the amphibole analyses for quartz diorite, were excluded from further estimation (Electronic Appendix Table A4). The thermometer of Putirka (2016) was used for comparison. Because the amphibole hygrometer was derived from Ridolfi & Renzulli (2012), which was deemed untenable by Erdmann *et al.* (2014), we also compared the results with those calculated from the plagioclase composition (see the plagioclase part of this section). The rock samples from the Portachuela batholith (Table 1) have mineral assemblages (amphibole + plagioclase + biotite + quartz + K–feldspar ± ilmenite–titanite + magnetite + apatite) similar to those of the experimental

tonalitic and granodioritic rocks. We therefore used the amphibole thermobarometer developed by Mutch *et al.* (2016) to estimate the emplacement pressure at the time of amphibole crystallization.

The results indicate that the amphibole grains crystallized under average pressures of 169 ± 29 MPa (SD, $n = 41$) for tonalite and under 105 ± 23 MPa (SD, $n = 28$) for quartz diorite (corresponding to average paleodepths of 6 ± 1 and 4 ± 1 km, respectively). According to the thermodynamic formula of Ridolfi (2021), the amphiboles in tonalite crystallized at average temperatures of 765 ± 14°C (SD, $n = 22$), consistent with the average
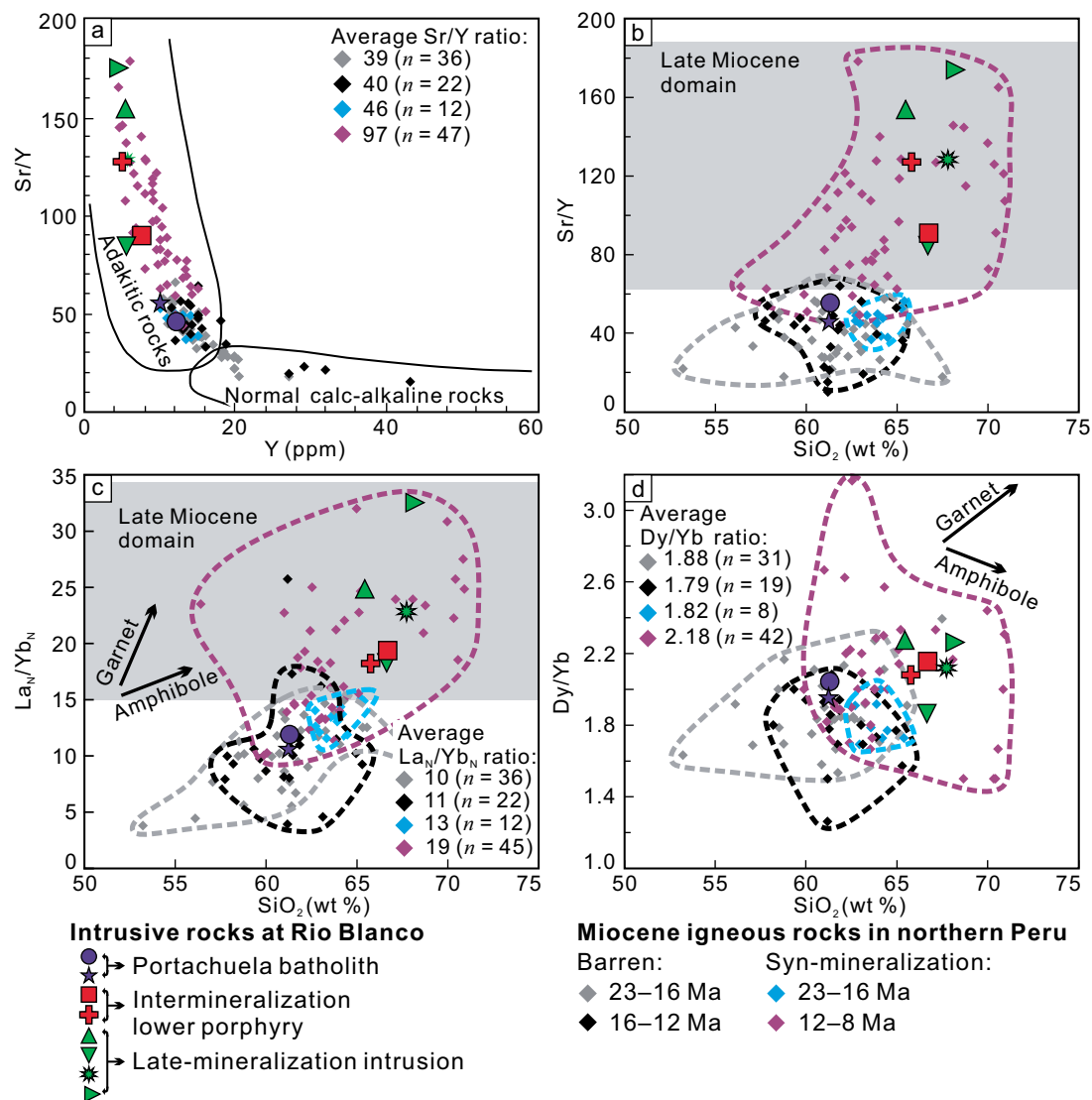
Fig. 9. Plots of (a) Sr/Y vs Y, (b) Sr/Y vs SiO₂, (c) La$_N$/Yb$_N$ vs SiO₂, and (d) Dy/Yb ratios vs SiO₂ contents of igneous rocks from Rio Blanco and northern Peru. Some 12–8 Ma syn-mineralization rocks have low Dy/Yb ratios, suggesting that amphibole fractionation also occurred. For the geochemical comparison, the Miocene igneous rocks in northern Peru are subdivided into four groups, namely 23–16 Ma (barren), 23–16 Ma (syn-mineralization), 16–12 Ma (barren), and 12–8 Ma (syn-mineralization).

crystallization temperature of $743 \pm 19°$C (SD, $n = 41$), which was obtained using the method of Putirka (2016). The crystallization temperatures of quartz diorite amphibole were $712 \pm 20°$C on average (SD, $n = 28$), as determined using the method of Putirka (2016; Electronic Appendix Table A4). The magmatic fO₂ content (oxygen fugacity) and H₂O content of tonalite calculated from the amphibole oxybarometer and hygrometer have average ΔFMQ$_{(amphibole)}$ values of $+1.4 \pm 0.2$ (SD, $n = 22$) and H₂O$_{(amphibole)}$ contents of 5.4 ± 0.2 wt % (SD, $n = 22$; Fig. 12).

Biotite

An Al-in-biotite thermobarometer for granitic rocks was employed to calculate the crystallization pressures of the biotite (Uchida *et al.*, 2007). The emplacement pressures at the time of biotite crystallization are 129 ± 15 MPa (SD, $n = 9$) for tonalite and 118 ± 21 MPa (SD, $n = 8$) for quartz

diorite; these are comparable with the pressures from the amphibole barometer. The crystallization pressures of biotite for the lower porphyry and porphyritic dacite 1 are 122 ± 21 MPa (SD, $n = 9$) and 229 ± 11 MPa (SD, $n = 8$), respectively.

Zircon

Data on the zircon trace-element abundances that may have been contaminated by mineral/melt inclusions were excluded using the following geochemical criteria: La >1 ppm and Ti >50 ppm (Lu *et al.,* 2016; Meng *et al.,* 2021b). The zircon crystallization temperatures for the samples were estimated using the Ti-in-zircon geothermometer developed by Loucks *et al.* (2020). An α_{SiO2} value of 1 was used because of the presence of igneous quartz in all of the studied samples. We adopted $\alpha_{TiO2} = 0.6$ because of the presence of Fe–Ti oxides in porphyry samples (Ferry & Watson, 2007;
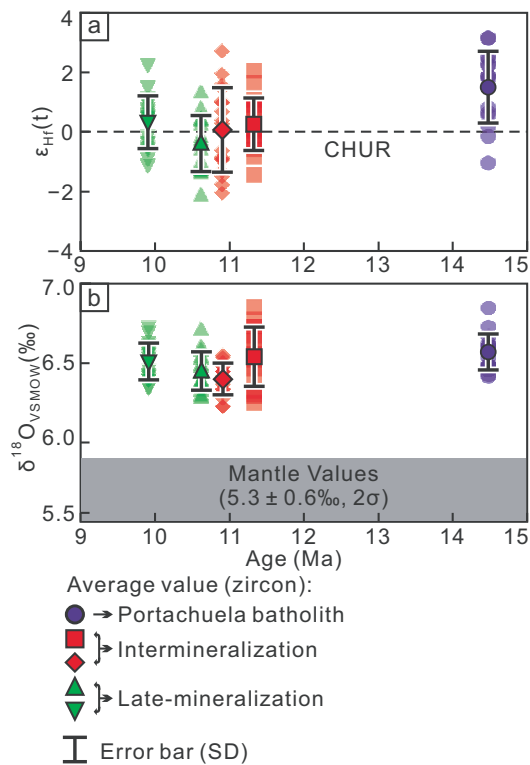
Fig. 10. (a) Initial $\varepsilon_{Hf}(t)_{(zircon)}$ and (b) $\delta^{18}O_{(zircon)}$ values against zircon U–Pb age of various intrusive rocks at Rio Blanco. CHUR = chondritic uniform reservoir. The mantle $\delta^{18}O_{(zircon)}$ value is from Valley *et al.* (1998).

Munoz *et al.*, 2012; Cao *et al.*, 2018b; Meng *et al.*, 2021b). The pressures were estimated using the amphibole (biotite) thermobarometer for the batholith (porphyry) samples. The results indicate that the average zircon crystallization temperatures decrease from $846 \pm 39°C$ (SD, $n = 16$) in tonalite to $766 \pm 43°C$ (SD, $n = 19$) in porphyritic dacite 1 (Fig. 12a).

Because of the difficulty of accurately measuring zircon La and Pr concentrations, we used the empirical method of Loucks *et al.* (2020) to calculate the magmatic fO_2. The initial U contents in zircon were calculated based on the zircon U contents and U–Pb ages reported by Chen *et al.* (2022). The results show that the Rio Blanco magmas yield increasing fO_2 values with time. The magmatic fO_2 values increase from ΔFMQ $+0.57 \pm 0.36$ (SD, $n = 16$) for tonalite to ΔFMQ $+1.38 \pm 0.63$ (SD, $n = 16$) for the younger quartz–plagioclase porphyry (Fig. 12b). This tendency of rising magmatic fO_2 with time also occurs in Miocene igneous rocks from the Yanacocha district, as revealed by the results calculated from the composition of amphibole and magnetite–ilmenite pairs (Fig. 12b; Chambefort *et al.*, 2013). In addition, our results indicate that the magmatic fO_2 calculated from the amphibole composition is higher than that from the zircon composition by 1–2 log units, consistent with previously published results (Wang *et al.*, 2014; Meng *et al.*, 2021b).

Plagioclase

The plagioclase–melt partition coefficient of Fe_2O_3 is about 9.5 times higher than that of FeO at X_{An} (mole fraction of anorthite [An]) ≈ 45 mol. % (Lundgaard & Tegner, 2004). Thus, the vast majority of iron is in the form of Fe^{3+} in plagioclase from the Rio Blanco intrusion. We report here the total Fe for simplification. The An and Fe contents of the plagioclase grains from tonalite and quartz diorite display relatively uniform profiles across the grains (Fig. 13a–c). The X_{An} values and Fe contents of the plagioclase in tonalite averaged 44 ± 3 mol. % (SD, $n = 20$) and 0.15 ± 0.02 wt % (SD, $n = 20$), respectively (Fig. 14a). The average plagioclase X_{An} values and Fe contents for quartz diorite are 40 ± 4 mol. % (SD, $n = 24$) and 0.15 ± 0.04 wt % (SD, $n = 24$), respectively (Fig. 14a).

A plagioclase hygrometer can be used to estimate the H_2O content of magmas (Lange *et al.*, 2009; Waters & Lange, 2015; Cheng *et al.*, 2020). However, the An in plagioclase is sensitive to magmatic water content and temperature but less sensitive to pressure. The pressures were estimated using the amphibole thermobarometer for the batholith samples and a biotite thermobarometer for porphyry samples, whereas the apatite saturation temperature (AST) and Ti-in-zircon temperature were used to constrain the temperature range at the time of plagioclase crystallization based on observation as follows. First, the presence of microcrystalline apatite in the cores of the plagioclase phenocrysts indicates that the apatite had become saturated when the plagioclase began to crystallize. Second, very few microcrystalline zircon grains are observed in the rims of the plagioclase phenocrysts, indicating that zircon crystallized at a late stage of plagioclase crystallization (Fig. 6f and g). Third, zircon grains separated from the batholith and porphyry samples contain abundant apatite inclusions, but the apatite grains do not contain zircon and other mineral inclusions (Electronic Appendix C). Therefore, the apatite and zircon grains crystallized mainly at an early stage and a late stage, respectively, with regard to plagioclase crystallization. Thus, the AST (Harrison & Watson, 1984) and Ti-in-zircon temperature (Tzrn; Loucks *et al.*, 2020; see results above) can constrain the maximum and minimum temperatures, respectively, at the time of plagioclase crystallization.

Experiments show that melts with ASI <1.1 have a similar apatite solubility to that of metaluminous melts (Piccoli & Candela, 2002). Assuming that the whole-rock SiO_2 and P_2O_5 concentrations represent the melt concentrations, we used samples with ASI <1.1 to estimate the AST (Harrison & Watson, 1984). Then, using the method of Bea *et al.* (1992), the ASTs are calculated to be 855°C–876°C (Table 3). The average magmatic $H_2O_{(AST)}$ contents are 6.2 ± 0.04 wt % (SD, $n = 20$) for tonalite and 6.1 ± 0.06 wt % (SD, $n = 24$) for quartz diorite (Fig. 15a). The average magmatic $H_2O_{(Tzrn)}$ contents are 6.6 ± 0.04 wt % (SD, $n = 20$) for tonalite and 6.5 ± 0.06 wt % (SD, $n = 24$) for quartz diorite (Fig. 15a).
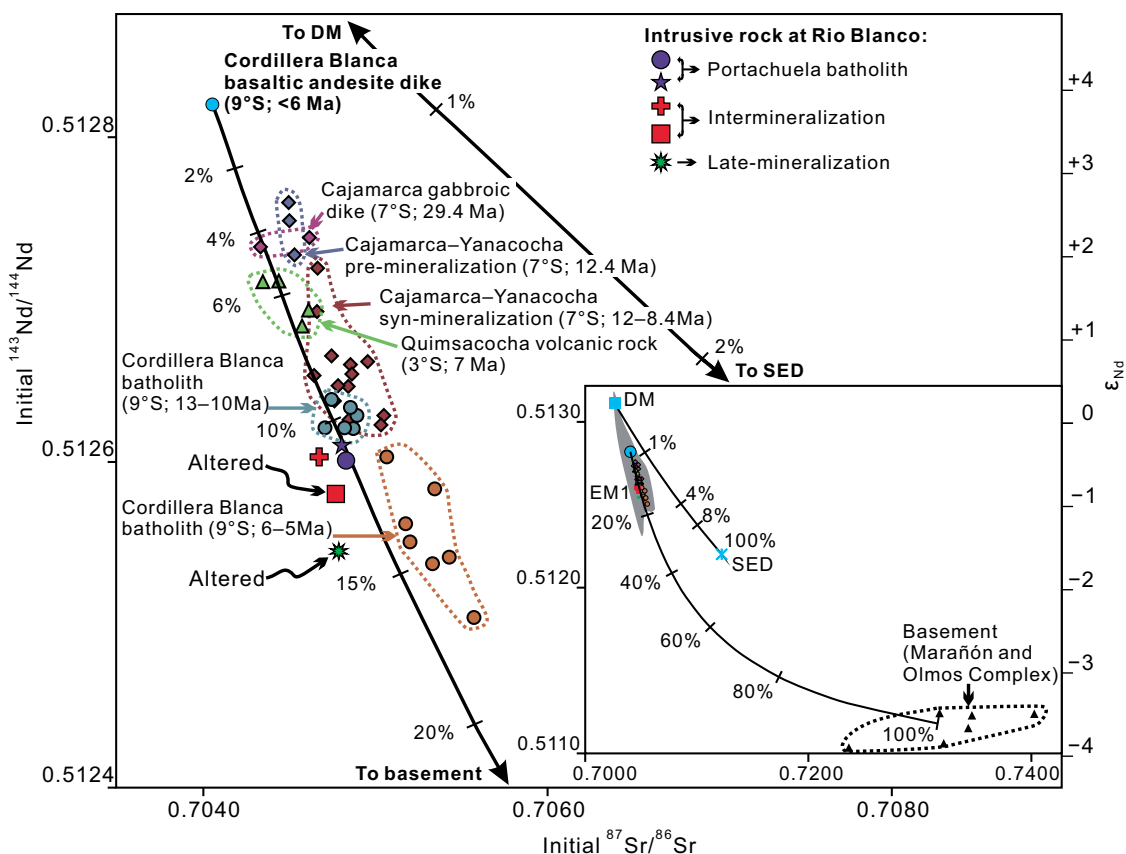
Fig. 11. Whole-rock Sr–Nd isotopes of Rio Blanco intrusive rocks and data on other igneous rocks in northern Peru (data from Petford & Atherton, 1996; Macfarlane, 1999; Davies, 2002; Chiaradia *et al.*, 2009a; Schütte, 2009). DM = depleted mantle, from Workman & Hart (2005); SED = global subducting sediment (GLOSS-II) composition, from Plank (2014); EM1 = enriched mantle 1, from Wieser *et al.* (2019).
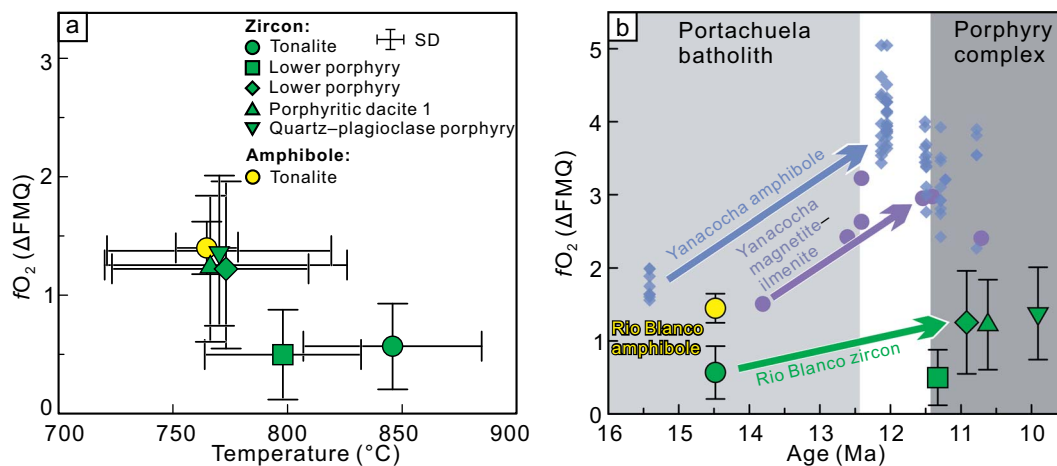

Fig. 12. (a) Magmatic fO_2 (in log units relative to FMQ; FMQ = fayalite–magnetite–quartz redox buffer) vs temperature. (b) Magmatic fO_2 values vs time. Magmatic fO_2 values calculated from the amphibole composition (method of Ridolfi, 2021) and magnetite–ilmenite pair in the Yanacocha district are shown for comparison.

Reverse zoning is common in the plagioclase phenocrysts in the intermineralization lower porphyry (Fig. 13d–i). The compositional profiles of the plagioclase phenocrysts suggest that the plagioclase cores have uniform X_{An} values (37 ± 4 mol. % on average, SD, $n = 90$) and Fe contents (0.13 ± 0.02 wt % on average, SD, $n = 90$; Figs 13d–i, 14a and b). The mantles of the plagioclase phenocrysts show the highest X_{An} values (mostly 52–

66 mol. %) and Fe contents (0.13–0.20 wt %), with average values of 56 ± 6 mol. % (SD, $n = 37$) and 0.15 ± 0.02 wt % (SD, $n = 37$), respectively (Figs 13d–i, 14a and b). As shown in the representative plagioclase elemental profiles (Fig. 13f), the X_{An} and Fe contents abruptly increase from the core (35 mol. % and 0.12 wt %, respectively) to the mantle (up to 59 mol. % and 0.20 wt %, respectively). At the rims of the plagioclase phenocrysts, X_{An} significantly
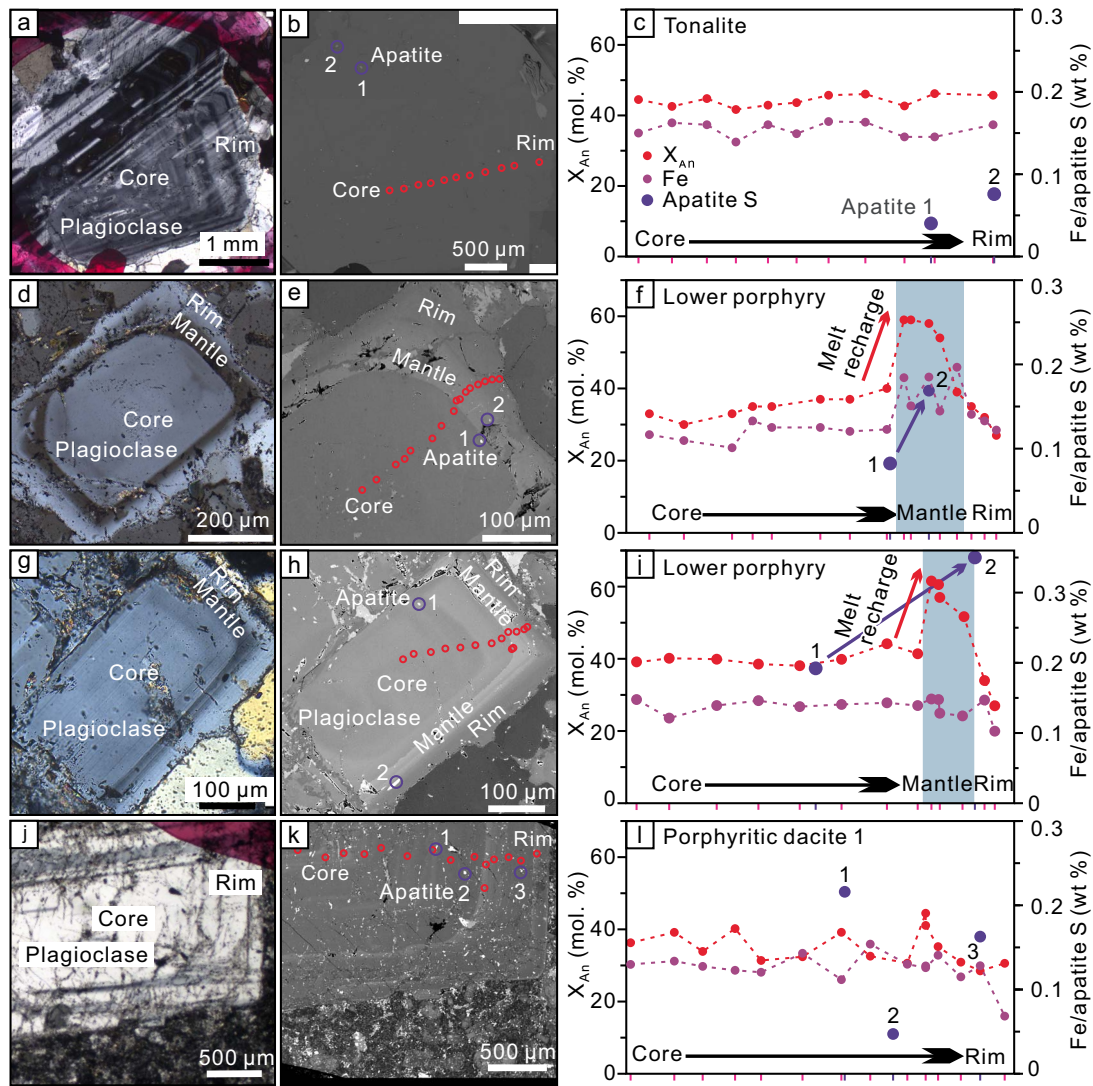
Fig. 13. Photomicrographs (cross-polarized transmitted light), BSE images, and electron microprobe analysis profiles of X_{An} and Fe contents for representative plagioclase crystals in (a–c) tonalite, (d–i) intermineralization lower porphyry, and (j–l) late-mineralization porphyritic dacite 1. The red circles in the BSE images denote the analyzed spots of plagioclase, and the blue circles are the analyzed spots of apatite inclusions in the plagioclase.

decreases to an average value of 26 ± 7 mol. % (SD, $n = 29$), but the Fe content remains nearly constant, with an average value of 0.13 ± 0.02 wt % (SD, $n = 29$), which is comparable with that in the cores of plagioclase phenocrysts (Figs 13d–i, 14a and b). The average magmatic $H_2O_{(AST)}$ content for lower porphyry is 6.3 ± 0.17 wt % (SD, $n = 156$; Fig. 15a). The average magmatic $H_2O_{(Tzrn)}$ content calculated from the Ti-in-zircon temperature is 7.6 ± 0.17 wt % (SD, $n = 156$; Fig. 15a).

The plagioclase phenocrysts in porphyritic dacite 1 of the late-mineralization intrusion have an average X_{An} value of 35 ± 4 mol. % (SD, $n = 29$) and Fe content of 0.12 ± 0.02 wt % (SD, $n = 29$), respectively (Fig. 14a). Only weak reverse zoning locally occurs in plagioclase phenocrysts with X_{An} values up to ca. 45 mol. % (Fig. 13j–l). The calculated magmatic $H_2O_{(AST)}$ content is 5.7 ± 0.07 wt % (SD, $n = 29$), whereas the $H_2O_{(Tzrn)}$ content is 8.5 ± 0.07 wt % on average (SD, $n = 29$; Fig. 15a). The plagioclase phenocrysts from porphyritic dacite 2

have the lowest X_{An} values (average of 30 ± 3 mol. %, SD, $n = 5$) and Fe contents (average of 0.13 ± 0.01 wt %, SD, $n = 5$; Fig. 14a). They also do not show reverse zoning. The calculated average magmatic $H_2O_{(AST)}$ and $H_2O_{(Tzrn)}$ contents of porphyritic dacite 2 are 5.3 ± 0.05 wt % (SD, $n = 5$) and 7.9 ± 0.05 wt % (SD, $n = 5$; Fig. 15a), respectively.

Apatite

The S and Cl contents of the igneous apatite grains are illustrated in Fig. 14c and d. We calculated the S content of magmas related to various intrusive phases. The S partition coefficient between apatite and melt is mainly controlled by magmatic fO_2 and temperature (Peng *et al.*, 1997; Streck & Dilles, 1998; Parat *et al.*, 2011; Hutchinson, 2019), so we used the method of Meng *et al.* (2021a) to compute the S partition coefficient ($D_S^{apatite/melt}$) as a function of magmatic fO_2 (Konecke *et al.*, 2017, 2019) and temperature (Parat & Holtz, 2004). The calculated
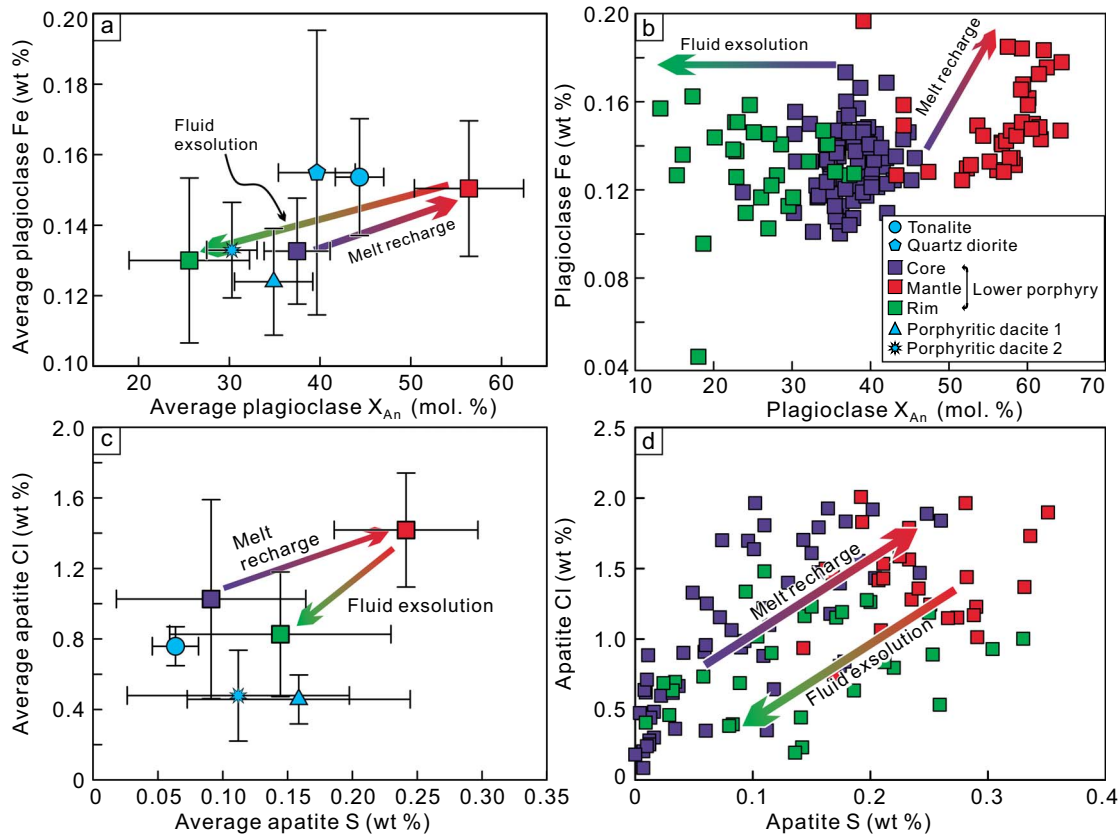
Fig. 14. (a) Average Fe contents vs X_{An} values in the plagioclase of Rio Blanco intrusions. (b) Fe contents vs X_{An} values in the plagioclase phenocrysts of the intermineralization lower porphyry. The X_{An} values are positively correlated with the Fe contents of the plagioclase mantles. The plagioclase rim has low X_{An} values, but the Fe contents remain constant. (c) Average Cl contents vs S contents of apatites in plagioclase phenocrysts of Rio Blanco intrusions. (d) Cl contents vs S contents of apatites in plagioclase phenocrysts of the intermineralization lower porphyry. The apatite in the plagioclase mantles has the highest S and Cl contents.
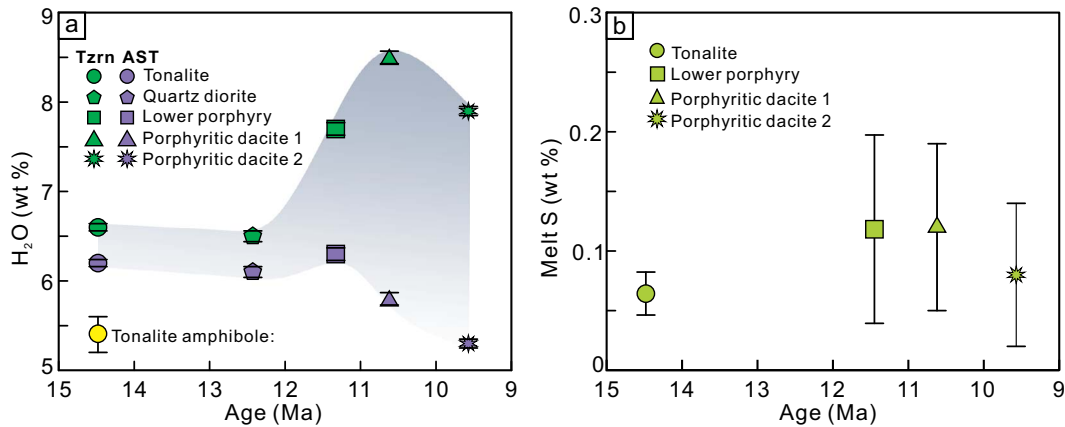
Fig. 15. Calculated (a) magmatic H_2O and (b) magmatic S contents against the timing of emplacement of Rio Blanco magmas.

$D_S^{apatite/melt}$ was used to estimate the melt S contents of the samples.

The tonalite apatite grains have an average S content of 0.06 ± 0.02 wt % (SD, $n = 9$) and average Cl content of 0.76 ± 0.11 wt % (SD, $n = 9$; Fig. 14c). The calculated melt S content is 0.06 ± 0.02 wt % on average (SD, $n = 9$; Fig. 15).

For the intermineralization lower porphyry, the S and Cl contents of the apatite exhibit a large core–mantle–rim variability (Fig. 14c and d). In each plagioclase phenocryst, the apatite S content of the mantle is

consistently higher than those in the cores (Fig. 13f and i; see Data Electronic Appendix D for details). In the cores of the plagioclase phenocrysts, the average S content of the apatite inclusions is 0.09 ± 0.07 wt % (SD, $n = 56$), whereas the average Cl content is 1.03 ± 0.56 wt% (SD, $n = 56$; Fig. 14c and d). The highest apatite S and Cl contents were obtained from the mantles of the plagioclase phenocrysts; their averages are 0.24 ± 0.06 wt % (SD, $n = 26$) and 1.42 ± 0.32 wt % (SD, $n = 26$), respectively (Fig. 14c and d). In the rims of the plagioclase phe-

nocrysts, the apatite S content averages 0.14 ± 0.09 wt % (SD, $n = 30$) and the Cl content averages 0.83 ± 0.35 wt % (SD, $n = 30$; Fig. 14c and d). The melt S content of the lower porphyry is 0.12 ± 0.08 wt % on average (SD, $n = 112$), which is significantly higher than the melt S content of tonalite (Fig. 15b).

The apatite grains in the late-mineralization porphyritic dacite 1 and 2 have low average S contents of 0.16 ± 0.09 wt % (SD, $n = 14$) and 0.11 ± 0.09 wt % (SD, $n = 3$) and low average Cl contents of 0.46 ± 0.14 wt % (SD, $n = 14$) and 0.48 ± 0.26 wt % (SD, $n = 3$; Fig. 14c). The melt S contents of porphyritic dacite 1 and 2 are 0.12 ± 0.07 wt % (SD, $n = 14$) and 0.08 ± 0.06 wt % (SD, $n = 3$) on average, respectively (Fig. 15).

DISCUSSION
Petrogenesis

The igneous rocks at Rio Blanco exhibit a strong enrichment in LILEs (e.g. Rb, Ba, Th, and K), depletion of HFSEs (e.g. Nb and Ta), and a negative Ti anomaly (Fig. 8a). These geochemical features are typical of subduction zone magmas. The Portachuela batholith has a relatively low Sr/Y ratio (46–55; Fig. 9a), no negative Eu anomaly, and flat REE patterns. These characterize Cenozoic magmas generated under moderate crustal thickness (amphibole ± plagioclase-stable field) and normal subduction in the Andes (Davies, 2002; Haschke *et al.*, 2002; Hollings *et al.*, 2005). In comparison, the Rio Blanco porphyry complex has a higher Sr/Y ratio of 85–175 (Fig. 9a) and steeper REE patterns (Fig. 8b). The compiled dataset suggests that this feature is common among igneous rocks emplaced between ca. 23 and 8 Ma in northern Peru (Fig. 9). The Sr/Y, La_N/Yb_N, and Dy/Yb ratios abruptly increased from ca. 41 to ca. 97, ca. 11 to ca. 19, and ca. 1.8 to ca. 2.2, respectively, at ca. 12 Ma. Previous studies propose the following genetic models elucidating the origin of adakitic magma: (1) partial slab melting and subsequent interactions with the mantle wedge (Bourdon *et al.*, 2002, 2003; Samaniego *et al.*, 2005, 2010; Hidalgo *et al.*, 2007); (2) crustal melting and/or assimilation of lower crustal rocks (Atherton & Petford, 1993; Garrison & Davidson, 2003); and/or (3) high-pressure fractionation of garnet and/or amphibole in the lower crust (Bryant *et al.*, 2006; Macpherson *et al.*, 2006; Chiaradia, 2009, 2015; Chiaradia *et al.*, 2009b; Richards, 2011a; Richards *et al.*, 2012).

The partial melting of young oceanic slab (≤5 Ma) is a general model for adakite genesis (Peacock *et al.*, 1994; Richards, 2011b). However, the Nazca slab is too old (>30 Ma) to have been implicated in such melting during normal-angle subduction (Atherton & Petford, 1993; Gutscher *et al.*, 1999), as a subducted slab is not heated to melting prior to dehydration (Peacock, 1996; Arcay *et al.*, 2007; Richards, 2011b). In another possible mechanism, the subduction of an oceanic plateau increases the amount of oceanic sediment and subduction erosion into the mantle wedge, which further

promotes the formation of porphyry-type deposits (Hollings *et al.*, 2005). However, if this process were indeed responsible for the lithogeochemical differences between the batholith and porphyry complex rocks at Rio Blanco, even in northern Peru (23–12 and 12–8 Ma), it would have resulted in distinct isotopic signatures, which is not supported by our indistinguishable, homogeneous zircon Hf–O isotopic data (Fig. 10). The comparable whole-rock Sr–Nd isotopes between the Portachuela batholith and the Rio Blanco porphyry complex also discount this mechanism (Fig. 11). Thus, the Rio Blanco porphyry complex and Late Miocene igneous rocks in northern Peru are more closely aligned with a 'continental adakite' rather than one produced from slab melting (Zhang *et al.*, 2004; Moyen, 2009; Montgomery, 2012).

The coherent trace and REE patterns and homogeneous isotopic values indicate that the Rio Blanco magmas evolved from a stable isotopic reservoir (Figs 8 and 10). These characteristics are also observed in igneous rocks from El Teniente (6.3–4.3 Ma), which formed during the subduction of the Juan Fernández Ridge in northern Chile (Maksaev *et al.*, 2004; Munoz *et al.*, 2012), and Yanacocha (12.3–8.4 Ma), which formed during the subduction of the Inca Oceanic Plateau in northern Peru (Chiaradia *et al.*, 2009a; Chambefort *et al.*, 2013). Petford *et al.* (1996) proposed that the Cordillera Blanca batholith evolved from an enriched subcontinental lithospheric mantle (SCLM) source (EM1 type; Fig. 11). Recent studies suggest that EM1-type mantle sources are also present in the Andean Southern Volcanic Zone (33°S–46°S; Turner *et al.*, 2017; Wieser *et al.*, 2019). Such mantle sources may arise from the recycling of metasomatized SCLM (M-SCLM), which causes heterogeneity in mantle wedges (Turner *et al.*, 2017). The mantle wedge heterogeneity in northern Peru may be reflected by the Sr–Nd isotopic variations in basaltic rocks (Cordillera Blanca basaltic andesite dike and Cajamarca gabbroic dike; Fig. 11). These igneous rock samples exhibit signs of mixing with basement rocks, suggesting that crustal contamination also contributed to the isotopic variations in northern Peru (Cajamarca mining district and Cordillera Blanca batholith; Fig. 11; Petford *et al.*, 1996; Davies, 2002; Chiaradia *et al.*, 2009a). Igneous rocks in Rio Blanco show narrow $\varepsilon_{Hf}(t)$ and $\delta^{18}O$ ranges of $+0.3 \pm 1.2$ (SD, $n = 86$) and $6.5 \pm 0.14‰$ (SD, $n = 86$; Fig. 10), respectively, suggesting a limited variation in the influence of crustal assimilation during magma ascent. The assimilation of mid- or upper-crustal rocks, which typically have elevated $\delta^{18}O$ values (e.g. up to 16‰ in the Eastern Cordillera basement; Hidalgo *et al.*, 2012), significantly increases $\delta^{18}O$ values and results in heterogeneous zircon Hf and O isotopic compositions between various intrusive units. This is also supported by the homogeneous whole-rock Sr–Nd isotopes in the least-altered rocks, indicating a 10%–12% crustal assimilation (Fig. 11). This observation is consistent with the different crustal thickening mechanisms occurring along the

South American continental margin. The northernmost part of Peru (ca. 5°S; at the latitude of the Rio Blanco district) exhibits minimal tectonic shortening, and the corresponding thickening is generally interpreted as a result of the underplating of mantle-derived basalt (Petford et al., 1996). The tectonic shortening progressively increases southward until it reaches ca. 20°S (Kley & Monaldi, 1998; Haschke & Gunther, 2003).

The Sr/Y, La$_N$/Yb$_N$, and Dy/Yb ratios of the igneous rocks in northern Peru remained constant at 23–12 Ma, but an abrupt increase occurred during the collision of the Inca Oceanic Plateau with the South American plate at ca. 12 Ma (Fig. 9). Amphibole and garnet have different partition coefficients for Dy and Yb, and fractionation of these two minerals leads to distinct Dy/Yb trends along magma differentiation. The Dy/Yb ratio decreases with amphibole fractionation but increases during garnet fractionation (Davidson et al., 2007). The fact that the whole-rock Dy/Yb ratios remained stable at 23–12 Ma but increased during the collision suggests that there has been a larger proportion of garnet cumulates in the source reservoir since ca. 12 Ma (Fig. 9d). Thus, the change in geochemical composition from normal calc-alkaline (to weakly adakitic) to significantly adakitic rocks is consistent with the transition from amphibole-stable to garnet-stable and plagioclase-poor cumulates mineral assemblage during fractionation in the source reservoir.

This transition coincided with the initial crustal thickening and decreasing subduction rate during the Quechua II orogeny in northern Peru (Noble et al., 1990; Sandeman et al., 1995; Chiaradia et al., 2009a; Michalak et al., 2016). The crustal thickening led to higher pressure, which may have promoted the garnet fractionation of mantle-derived magma in the hot zone at the crust–mantle boundary (Annen et al., 2006; Chiaradia, 2015; Farner & Lee, 2017). Chiaradia et al. (2009a) investigated the Yanacocha deposit in the Cajamarca district and stated that an increase in crustal compression caused magmas to stall in lower- to mid-crustal magma reservoirs, where amphibole and/or garnet is stable (Davidson et al., 2007). This may play a second-order role in increasing Sr/Y and La$_N$/Yb$_N$ ratios. This is indicated by the low Dy/Yb ratios in some of the 12–8 Ma igneous rocks in northern Peru (Fig. 9d).

We conclude that mantle-derived magmas mixed at the crust–mantle boundary (e.g. hot zone) to form a homogeneous isotopic reservoir. During the collision of the Inca Oceanic Plateau with the South American plate, the source magmas underwent high-pressure, garnet-stable fractionation. The increased arc compression caused magmas to stall in the lower- to mid-crustal magma chambers, promoted amphibole, and suppressed plagioclase fractionation. This scenario may explain the different geochemical characteristics between 23–12 and 12–8 Ma igneous rocks in northern Peru.

Recharge of volatile-rich melts and the porphyry mineralization

The amphibole and biotite compositions show that the Rio Blanco magmas crystallized mainly at relatively shallow depths (4–6 km), which is typical of ore-related intrusions in porphyry Cu systems (Sillitoe, 2010). The H$_2$O$_{(AST)}$ values are slightly higher than the H$_2$O$_{(Tzrn)}$ values estimated with the same plagioclase hygrometer (Fig. 15a; Waters & Lange, 2015). Apatite generally crystallizes earlier than zircon in granitic melts (Anderson et al., 2008), as supported in our study by the abundance of apatite inclusions in zircon grains and absence of zircon inclusion within the apatite grains (Electronic Appendix C). These observations are consistent with the higher AST values than the Ti-in-zircon crystallization temperatures for all of the samples. Magmatic H$_2$O content calculated from a plagioclase hygrometer is negatively correlated with the crystallization temperature. Hence, the common occurrence of apatite in the cores of plagioclase phenocrysts and the near-restriction of zircon grains in the rims of the plagioclase grains indicate that the H$_2$O values estimated using the AST and Ti-in-zircon temperature provide the minimum and maximum constraints, respectively, of the magmatic H$_2$O contents at the time of plagioclase crystallization. Our results suggest that the magma in the intermineralization lower porphyry is slightly more hydrous than that in the pre-mineralization tonalite and quartz diorite (Fig. 15a).

The results obtained from the amphibole and zircon Ti–Ce–U$_i$ oxybarometers are internally consistent and suggest that the Rio Blanco magmas were moderately oxidized (ΔFMQ +0.5; Fig. 12). Compared with the Portachuela batholith, the younger porphyritic rocks have higher magmatic fO$_2$ values, which may be common for magmas associated with the Late Miocene deposits in northern Peru; this is supported by results from an amphibole oxybarometer and magnetite–ilmenite pairs among samples from the Yanacocha district (Fig. 12b; Chambefort et al., 2013). The elevated magmatic fO$_2$ and H$_2$O content of ore-related magma at Rio Blanco are comparable with those of magmas associated with many other porphyry Cu deposits (e.g. Richards, 2015). High magmatic H$_2$O content promotes the crystallization of hydrous mafic minerals, mainly amphibole, and suppresses the crystallization of plagioclase (Naney, 1983; Moore & Carmichael, 1998), thus resulting in a high Sr content and low Y content of the evolved magma (Rohrlach & Loucks, 2005; Richards, 2011a; Richards et al., 2012). High magmatic fO$_2$ can dissolve and transport a large amount of oxidized S to upper-crustal magma chambers (Jugo et al., 2005; Wang et al., 2014; Richards, 2015; Lee & Tang, 2020; Tang et al., 2020).

Plagioclase reverse zoning is not observed in tonalite and quartz diorite but is generally seen in the intermineralization lower porphyry (Fig. 13d–i). In the cores of the plagioclase phenocrysts in the lower porphyry, the apatite S and Cl contents are slightly higher than those

of apatite grains in the tonalite samples (Fig. 14c). The S and Cl contents of the apatite grains hosted in the mantles of plagioclase phenocrysts are significantly higher than those of grains hosted in the cores (Fig. 14c and d). This may be attributed to the recharge of volatile-rich melts. The weak positive correlation between the X_{An} values and Fe contents of the mantles of plagioclase phenocrysts indicates that the replenishing melts could be relatively mafic (Fig. 14b). These results indicate that the recharge of volatile-rich melts was the main mechanism responsible for enhancing the magmatic S and Cl contents at Rio Blanco, as also supported by the elevated melt S content of the lower porphyry compared with that of the batholitic tonalite (Fig. 15).

X_{An} significantly decreases while Fe remains constant at the rims of plagioclase phenocrysts (Fig. 14b). The apatite S and Cl contents at the rims are significantly lower compared with those of the mantles of plagioclase phenocrysts (Fig. 14c and d). Melt differentiation/composition, temperature, pressure, and H_2O content influence the An content of plagioclase (Hattori & Sato, 1996; Ginibre *et al.,* 2002; Hammer & Rutherford, 2002; Ustunisik *et al.,* 2014). Melt differentiation decreases the An and Fe contents of plagioclase (Ginibre *et al.,* 2002), and this mechanism can be offset by a drop in An with stable Fe contents at the rims of plagioclase phenocrysts (Fig. 14b). Pressure fluctuation has a limited effect on the An content of plagioclase (Ustunisik *et al.,* 2014; Cao *et al.,* 2019). Thus, the sharp decrease in An content but nearly constant Fe content at the rims of plagioclase phenocrysts are plausibly explained by fluid exsolution during the quasi-isothermal ascent of fluid-saturated magma (Hattori & Sato, 1996; Zhang *et al.,* 2008; Frey & Lange, 2011; Giacomoni *et al.,* 2014). This is consistent with the low apatite S and Cl contents at the rims of plagioclase phenocrysts, as fluid exsolution significantly decreases the S concentration ($D_S^{fluid/melt} > 30$; Chelle-Michou *et al.,* 2017) and Cl concentration ($D_{Cl}^{fluid/melt} > 1$; Chelle-Michou *et al.,* 2017; Tattitch *et al.,* 2021) in melts. We therefore argue that the recharge of volatile-rich melts into the upper-crustal magma chamber was immediately followed by fluid exsolution at the time of emplacement of the intermineralization lower porphyry (Fig. 16). These findings are consistent with previous studies that suggest the importance of melt mixing in triggering fluid exsolution and subsequent formation of porphyry Cu deposits (Sparks & Marshall, 1986; Hattori & Sato, 1996; Hattori & Keith, 2001; Nadeau *et al.,* 2010; Wilkinson, 2013; Cao *et al.,* 2014, 2018a, 2018b; Blundy *et al.,* 2015; Zhu *et al.,* 2018). Volatile-rich melt recharge may also occur throughout the magmatic system history from ca. 12 to 8 Ma at the Yanacocha magmatic center, and it supplied abundant volatiles and metals to shallow magma chambers, significantly impacting mineralization (Chambefort *et al.,* 2008, 2013; Chiaradia *et al.,* 2009a).

Low apatite S and Cl contents indicate greater fluid exsolution from the magma chamber at the time of formation of late-mineralization intrusions than that of the intermineralization lower porphyry (Fig. 14). The limited fluctuations in the An content of plagioclase phenocrysts in porphyritic dacite 1 likely indicate that the oscillatory zoning was caused by internal crystal growth mechanisms (e.g. crystal growth rate, elemental diffusion, and elemental partitioning; cf. Cao *et al.,* 2019) or by insignificant variations in physiochemical conditions (e.g. temperature, pressure, fO_2, and melt composition; Singer *et al.,* 1995; Ginibre *et al.,* 2007). Thus, the melt recharge event ceased at the time of emplacement of late-mineralization intrusions (porphyritic dacite 1 and porphyritic dacite 2).

Genetic relationship between oceanic plateau subduction and porphyry Cu deposit formation

A spatiotemporal relationship has been identified between the subduction of topographic anomalies and the formation of porphyry ore deposits (Reich *et al.,* 2003; Cooke *et al.,* 2005; Rosenbaum *et al.,* 2005). At Rio Blanco, batholithic magmatism persisted from ca. 24 to 12.4 Ma and was followed by the emplacement of the ore-related porphyry complex from ca. 11.5 to 9 Ma (Fig. 4; Chen *et al.,* 2022). The isotopic results suggest that the Rio Blanco magmas evolved from an isotopically homogeneous magma reservoir (e.g. hot zone) at the crust–mantle boundary (Annen *et al.,* 2006). This reservoir may have been existing for approximately 10 million years prior to the collision of the Inca Oceanic Plateau at 12–10 Ma (Gutscher *et al.,* 1999).

The 24–12 Ma rocks from northern Peru (including the Portachuela batholith) have low Sr/Y, La_N/Yb_N, and Dy/Yb ratios (Fig. 9), whereas the 12–8 Ma igneous rocks (including the Rio Blanco porphyry complex) that formed during the subduction of the Inca Oceanic Plateau have comparable zircon Hf–O and whole-rock Sr–Nd isotopes but elevated Sr/Y, La_N/Yb_N, and Dy/Yb ratios, greater magmatic fO_2, and higher abundance of volatile elements. This rapid transition of geochemical characteristics of magmas since the collision of the Inca Oceanic Plateau may reflect the compressional states of stress and crustal thickening (Noble *et al.,* 1990; Chiaradia *et al.,* 2009a; Michalak *et al.,* 2016). Crustal thickening led to higher pressure in the magma reservoir at the crust–mantle boundary, promoting garnet fractionation in mantle-derived magma (Annen *et al.,* 2006; Chiaradia, 2015; Farner & Lee, 2017). Loucks (2021) stated that arc compression acts as a tectonic trap and contributes to the evolution of mantle-derived magmas at the crust–mantle boundary. In the scenario depicted by Loucks (2021), magmas generated under a normal subduction regime corresponded to 24–12 Ma igneous rocks in northern Peru (including the Portachuela batholith) that yielded a low SiO_2, a high Y, and low Sr/Y, La_N/Yb_N, and Dy/Yb ratios (Fig. 17a).

During the collision of the Inca Oceanic Plateau with the South American plate (Fig. 17b), the enhanced coupling led to quasi-instantaneous arc compression, which impeded magma ascent (Chiaradia, 2009; Chiaradia *et al.,*
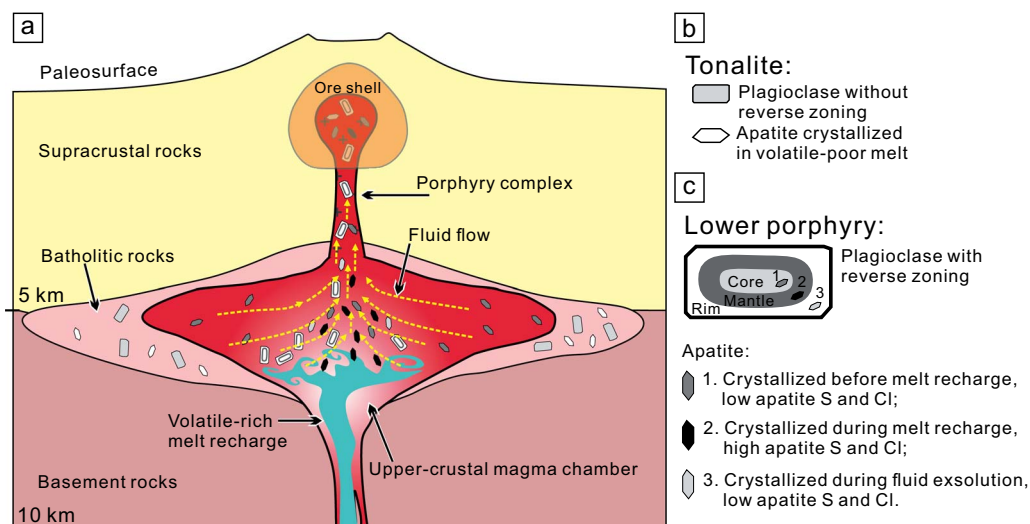
Fig. 16. (a) Schematic drawing of the recharge of volatile-rich melt into the upper-crustal magma chamber beneath Rio Blanco. This process was reconciled by reverse zoning in the plagioclase phenocrysts and the abundance of volatile elements in the apatite inclusions (modified from Richards, 2011b). (b) Characteristics of plagioclase and apatite crystals in pre-mineralization tonalite. Plagioclase does not show reverse zoning, and apatite crystallized in volatile-poor melt, with low S and Cl contents. (c) Characteristics of plagioclase and apatite crystals in intermineralization lower porphyry. Plagioclase exhibits reverse zoning and contains three types of apatite inclusions, namely those that crystallized before melt recharge, during melt recharge, and during fluid exsolution.
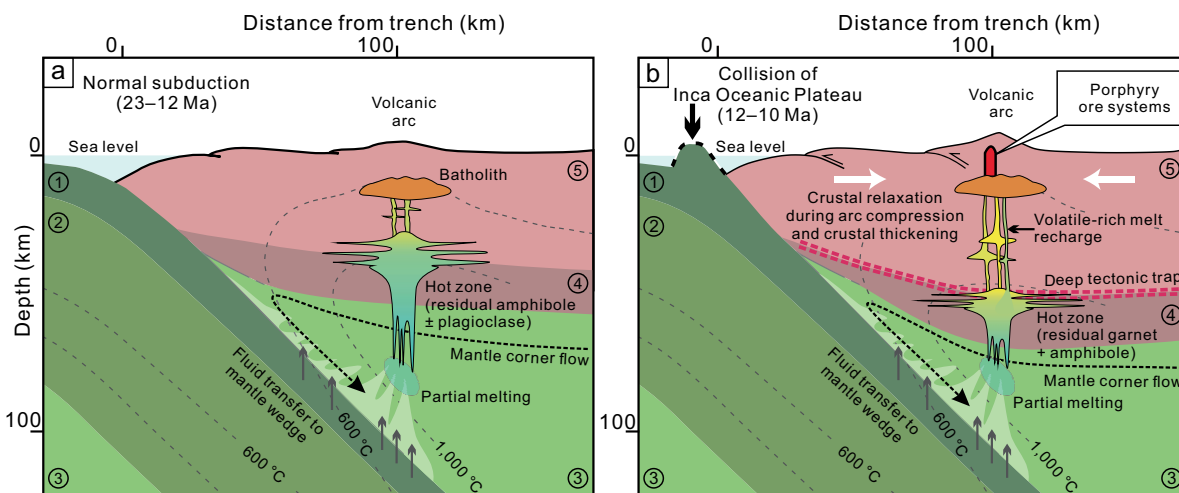
Fig. 17. Two-stage tectonic model of the magma evolution beneath Rio Blanco. (a) Magmas generated during normal subduction at 23–12 Ma. Mantle-derived magmas underwent amphibole ± plagioclase fractionation in the hot zone. (b) Collision of the Inca Oceanic Plateau with the South American plate and subsequent formation of porphyry deposits. The collision of the Inca Oceanic Plateau did not cause flat-slab subduction, but it increased horizontal compression and crustal thickness. Mantle-derived magmas underwent garnet + amphibole fractionation in the hot zone (modified from Wilkinson, 2013). ① Basaltic crust; ② lithospheric mantle; ③ asthenosphere, mantle flow; ④ subcontinental lithospheric mantle; ⑤ continental crust.

2009a, 2009b; Loucks, 2021) and enabled a long-term evolution of magmas at the crust–mantle boundary. Significant garnet and amphibole fractionation occurred during magmatic differentiation, as indicated by the elevated Sr/Y, La_N/Yb_N, and Dy/Yb ratios of 12–8 Ma igneous rocks in northern Peru (including the Rio Blanco porphyry complex; Fig. 9). Such fractionation of garnet and amphibole that are depleted in ferric iron (Lee & Tang, 2020; Zhang et al., 2022) may drive the relatively oxidized hydrous parental magmas to a higher magmatic fO_2 and sulfur content, as suggested by our estimation of these parameters for porphyritic magmas compared with those for the batholith.

Cooke et al. (2005) concluded that the subduction of topographic anomalies acts as a tectonic perturbation that triggers the formation of porphyry Cu deposits. Considering crustal compression typically impedes magma ascent (Loucks, 2021), we suggest here that a transient change in regional stress (e.g. crustal relaxation) during the collision of Inca Oceanic Plateau allowed a high magma flux after a period of magma ascent impediment. The high magma flux may have resulted in the magma replenishment that is associated with porphyry Cu deposits in the Andes (Caricchi et al., 2014; Schöpa et al., 2017; Cox et al., 2020), which is supported by plagioclase reverse zoning in the samples of the

intermineralization lower porphyry from Rio Blanco (Fig. 16) and Yanacocha (Chiaradia *et al.,* 2009a; Chambefort *et al.,* 2013). Replenishment of the volatile-rich magma may destabilize the upper-crustal magma chamber (Blundy *et al.,* 2015; Richards, 2018) and trigger fluid supersaturation and exsolution that will ultimately lead to porphyry Cu mineralization (Audétat & Simon, 2012; Wilkinson, 2013; Blundy *et al.,* 2015; Richards, 2018; Korges *et al.,* 2020).

Hence, we suggest that arc compression associated with the collision of the Inca Oceanic Plateau promotes the magma fertility and a transient change of stress state is a dominant tectonic trigger (Cooke *et al.,* 2005; Loucks, 2021) of the formation of Rio Blanco. This scenario may also explain the formation of other porphyry ore systems associated with the subduction of topographic anomalies.

CONCLUSIONS

This petrogenetic study assesses the genetic relationship between the subduction of the Inca Oceanic Plateau and the formation of the giant porphyry Cu deposit at Rio Blanco. Our systematic geochemical analysis suggests that the Rio Blanco magmas evolved from a long-lived, isotopically stable, homogeneous reservoir at the crust–mantle boundary. This magmatic reservoir might have been existing for ca. 10 m.y. before the collision of the Inca Oceanic Plateau. At the time of collision, the mantle-derived magma became more evolved, relatively oxidized, and volatile-rich, making it conductive to porphyry deposit formation. Our results also imply that the Late Miocene igneous rocks in northern Peru, including those of the Rio Blanco porphyry complex, were generated during this period of tectonic transition. The crustal thickening and arc compression regime provided favorable conditions for mantle-derived magmas to evolve as relatively oxidized, volatile-rich magmas that ultimately emplaced at upper crustal level and formed porphyry ore systems.

SUPPLEMENTARY DATA

Supplementary data for this paper are available at *Journal of Petrology* online.

References

Anderson, J. L., Barth, A. P., Wooden, J. L. & Mazdab, F. (2008). Thermometers and thermobarometers in granitic systems. *Reviews in Mineralogy and Geochemistry* **69**, 121–142.

Annen, C., Blundy, J. D. & Sparks, R. S. J. (2006). The genesis of intermediate and silicic magmas in deep crustal hot zones. *Journal of Petrology* **47**, 505–539.

Arcay, D., Tric, E. & Doin, M. P. (2007). Slab surface temperature in subduction zones: influence of the interplate decoupling depth and upper plate thinning processes. *Earth and Planetary Science Letters* **255**, 324–338.

Atherton, M. P. & Petford, N. (1993). Generation of sodium-rich magmas from newly underplated basaltic crust. *Nature* **362**, 144–146.

Audétat, A. & Simon, A. C. (2012) Magmatic controls on porphyry Cu genesis. In: Hedenquist, J. W., Harris, M. & Camus, F. (eds)*Geology and Genesis of Major Copper Deposits and Districts of the World: a Tribute to Richard Sillitoe. Society of Economic Geologists, Special Publication*, **16**, 553–572.

Baertschi, P. (1976). Absolute ^{18}O content of standard mean ocean water. *Earth and Planetary Science Letters* **31**, 341–344.

Bea, F., Fershtater, G. & Corretgé, L. (1992). The geochemistry of phosphorus in granite rocks and the effect of aluminium. *Lithos* **29**, 43–56.

Beas, B. (2015) Volcanic stratigraphy at La Zanja Mining District in the northern Peruvian Andes, Cajamarca, Peru. M. Sc thesis, University of Tasmania, Tasmania, Australia, p. 289..

Blichert-Toft, J. & Albarède, F. (1997). The Lu-Hf isotope geochemistry of chondrites and the evolution of the mantle-crust system. *Earth and Planetary Science Letters* **148**, 243–258.

Blundy, J., Mavrogenes, J., Tattitch, B., Sparks, S. & Gilmer, A. (2015). Generation of porphyry copper deposits by gas–brine reaction in volcanic arcs. *Nature Geoscience* **8**, 235–240.

Bourdon, E., Eissen, J. P., Monzier, M., Robin, C., Martin, H., Cotten, J. & Hall, M. L. (2002). Adakite-like lavas from Antisana Volcano (Ecuador): evidence for slab melt metasomatism beneath Andean Northern Volcanic Zone. *Journal of Petrology* **43**, 199–217.

Bourdon, E., Eissen, J. P., Gutscher, M. A., Monzier, M., Hall, M. L. & Cotten, J. (2003). Magmatic response to early aseismic ridge subduction: the Ecuadorian margin case (South America). *Earth and Planetary Science Letters* **205**, 123–138.

Bristow, A. & Pratt, W. T. (2005). El proyecto de Cu–Mo Rio Blanco conferencias powerpoint. *Congreso Internacional de Prospectores y Exploradores* **4**, 59.

Bryant, J. A., Yogodzinski, G. M., Hall, M. L., Lewicki, J. L. & Bailey, D. G. (2006). Geochemical constraints on the origin of volcanic rocks from the Andean Northern Volcanic Zone, Ecuador. *Journal of Petrology* **47**, 1147–1175.

Cao, M. J., Qin, K. Z., Li, G. M., Yang, Y. H., Evans, N. J., Zhang, R. & Jin, L. Y. (2014). Magmatic process recorded in plagioclase at the Baogutu reduced porphyry Cu deposit, western Junggar, NW-China. *Journal of Asian Earth Sciences* **82**, 136–150.

Cao, M. J., Evans, N. J., Hollings, P., Cooke, D. R., McInnes, B. I. A., Qin, K. & Li, G. M. (2018a). Phenocryst zonation in porphyry-related

rocks of the Baguio district, Philippines: evidence for magmatic and metallogenic processes. *Journal of Petrology* **59**, 825–848.

Cao, M. J., Hollings, P., Cooke, D. R., Evans, N. J., McInnes, B. I. A., Qin, K. Z., Li, G. M., Sweet, G. & Baker, M. (2018b). Physicochemical processes in the magma chamber under the Black Mountain porphyry Cu-Au deposit, Philippines: insights from mineral chemistry and implications for mineralization. *Economic Geology* **113**, 63–82.

Cao, M. J., Evans, N. J., Reddy, S. M., Fougerouse, D., Hollings, P., Saxey, D. W., McInnes, B. I. A., Cooke, D. R., McDonald, B. J. & Qin, K. Z. (2019). Micro- and nano-scale textural and compositional zonation in plagioclase at the Black Mountain porphyry Cu deposit: implications for magmatic processes. *American Mineralogist* **104**, 391–402.

Cao, M. J., Evans, N. J., Hollings, P., Cooke, D. R., McInnes, B. I. A. & Qin, K. Z. (2021). Apatite texture, composition, and O-Sr-Nd isotope signatures record magmatic and hydrothermal fluid characteristics at the Black Mountain porphyry deposit, Philippines. *Economic Geology* **116**, 1189–1207.

Cardona, A., Cordani, U. G., Ruiz, J., Valencia, V., Nutman, A. & Sanchez, A. (2006). U/Pb detrital zircon geochronology and Nd isotopes from paleozoic metasedimentary rocks of the Marañón complex: insights on the proto-Andean tectonic evolution of the eastern Peruvian Andes. *Journal of Geology* **117**, 285–305.

Cardona, A., Cordani, U. G., Ruiz, J., Valencia, V. A., Armstrong, R., Chew, D., Nutman, A. & Sanchez, A. W. (2009). U-Pb zircon geochronology and Nd isotopic signatures of the pre-Mesozoic metamorphic basement of the eastern Peruvian Andes: growth and provenance of a Late Neoproterozoic to carboniferous accretionary orogen on the northwest margin of Gondwana. *Journal of Geology* **117**, 285–305.

Caricchi, L., Simpson, G. & Schaltegger, U. (2014). Zircons reveal magma fluxes in the Earth's crust. *Nature* **511**, 457–461.

Carrasquero, S. I., Rubinstein, N. A., Gómez, A. L. R., Chiaradia, M., Fontignie, D. & Valencia, V. A. (2018). New insights into petrogenesis of Miocene magmatism associated with porphyry copper deposits of the Andean Pampean flat slab, Argentina. *Geoscience Frontiers* **9**, 1565–1576.

Cashman, K. V., Sparks, R. S. J. & Blundy, J. D. (2017). Vertically extensive and unstable magmatic systems: a unified view of igneous processes. *Science* **355**, 355.

Chambefort, I., Dilles, J. H. & Kent, A. J. R. (2008). Anhydrite-bearing andesite and dacite as a source for sulfur in magmatic-hydrothermal mineral deposits. *Geology* **36**, 719–722.

Chambefort, I., Dilles, J. H. & Longo, A. A. (2013). Amphibole geochemistry of the Yanacocha Volcanics, Peru: evidence for diverse sources of magmatic volatiles related to gold ores. *Journal of Petrology* **54**, 1017–1046.

Chelle-Michou, C., Rottier, B., Caricchi, L. & Simpson, G. (2017). Tempo of magma degassing and the genesis of porphyry copper deposits. *Scientific Reports* **7**, 40566.

Chen, N., Pratt, W., Mao, J. W., Xie, G. Q., Moisy, M., Santos, A., Guo, W. M., Zheng, W. & Liu, J. N. (2022) *Economic Geology*. Northern Peru.

Cheng, Z. G., Zhang, Z. C., Chai, F. G., Hou, T., Santosh, M., Turesebekov, A. & Nurtaev, B. S. (2018). Carboniferous porphyry Cu–Au deposits in the Almalyk orefield, Uzbekistan: the Sarycheku and Kalmakyr examples. *International Geology Review* **60**, 1–20.

Cheng, Z. G., Zhang, Z. C., Wang, Z. C., Wang, F. Y., Mao, Q., Xu, L. J., Ke, S., Yu, H. M. & Santosh, M. (2020). Petrogenesis of transitional large igneous province: insights from bimodal volcanic suite in the Tarim large igneous province. *Journal of Geophysical Research: Solid Earth* **125**, e2019JB018382.

Chew, D. M., Schaltegger, U., Košler, J., Whitehouse, M. J., Gutjahr, M., Spikings, R. A. & Mišković, A. (2007). U-Pb geochronologic evidence for the evolution of the Gondwanan margin of the north-Central Andes. *Geological Society of America Bulletin* **119**, 697–711.

Chew, D. M., Pedemonte, G. & Corbett, E. (2016). Proto-Andean evolution of the Eastern Cordillera of Peru. *Gondwana Research* **35**, 59–78.

Chiaradia, M. (2009). Adakite-like magmas from fractional crystallization and melting-assimilation of mafic lower crust (Eocene Macuchi arc, Western cordillera, Ecuador). *Chemical Geology* **265**, 468–487.

Chiaradia, M. (2015). Crustal thickness control on Sr/Y signatures of recent arc magmas: an Earth scale perspective. *Scientific Reports* **5**, 1–5.

Chiaradia, M., Merino, D. & Spikings, R. (2009a). Rapid transition to long-lived deep crustal magmatic maturation and the formation of giant porphyry-related mineralization (Yanacocha, Peru). *Earth and Planetary Science Letters* **288**, 505–515.

Chiaradia, M., Müntener, O., Beate, B. & Fontignie, D. (2009b). Adakite-like volcanism of Ecuador: lower crust magmatic evolution and recycling. *Contributions to Mineralogy and Petrology* **158**, 563–588.

Chu, N. C., Taylor, R. N., Chavagnac, V., Nesbitt, R. W., Boella, R. M., Milton, J. A., German, C. R., Bayon, G. & Burton, K. (2002). Hf isotope ratio analysis using multi-collector inductively coupled plasma mass spectrometry: an evaluation of isobaric interference corrections. *Journal of Analytical Atomic Spectrometry* **17**, 1567–1574.

Coba, L., Callo, W. & Mamani, M. (2018) *Mapa Geologico del Perú, Escala 1: 1,000,000*. Lima, Peru: Insitituto Geológico, Minero y Metalúrgico.

Coira, B., Davidson, J., Mpodozis, C. & Ramos, V. (1982). Tectonic and magmatic evolution of the Andes of northern Argentina and Chile. *Earth-Science Reviews* **18**, 303–332.

Cooke, D. R., Hollings, P. & Walshe, J. L. (2005). Giant porphyry deposits: characteristics, distribution, and tectonic controls. *Economic Geology* **100**, 801–818.

Cox, D., Watt, S. F. L., Jenner, F. E., Hastie, A. R., Hammond, S. J. & Kunz, B. E. (2020). Elevated magma fluxes deliver high-Cu magmas to the upper crust. *Geology* **48**, 957–960.

Davidson, J., Turner, S., Handley, H., Macpherson, C. & Dosseto, A. (2007). Amphibole "sponge" in arc crust? *Geology* **35**, 787–790.

Davies, R. C. (2002) Tectonic, magmatic and metallogenic evolution of the Cajamarca mining district, Northern Peru. Ph.D. thesis, James Cook University, Australia, p. 323.

Davies, R. C. & Williams, P. J. (2005). The El Galeno and Michiquillay porphyry Cu–Au–Mo deposits: geological descriptions and comparison of Miocene porphyry systems in the Cajamarca district, northern Peru. *Mineralium Deposita* **40**, 598–616.

Defant, M. J. & Drummond, M. S. (1990). Derivation of some modern arc magmas by melting of young subducted lithosphere. *Nature* **347**, 662–665.

Díaz, N., Jiménez, C., Alva, C., Macharé, J., Cánepa, C. & Injoque, J. (1997) *Estudio geoquímico de orientación del depósito pórfido de cobre La Granja. Resúmenes IX Congreso Peruano de Geología*, pp.25–30.

Erdmann, S., Martel, C., Pichavant, M. & Kushnir, A. (2014). Amphibole as an archivist of magmatic crystallization conditions: problems, potential, and implications for inferring magma storage prior to the paroxysmal 2010 eruption of Mount Merapi, Indonesia. *Contributions to Mineralogy and Petrology* **167**, 1–23.

Farner, M. J. & Lee, C. T. A. (2017). Effects of crustal thickness on magmatic differentiation in subduction zone volcanism: a global study. *Earth and Planetary Science Letters* **470**, 96–107.

Feininger, T. (1982). The metamorphic "basement" of Ecuador. *Geological Society of America Bulletin* **93**, 87–92.

Ferry, J. M. & Watson, E. B. (2007). New thermodynamic models and revised calibrations for the Ti-in-zircon and Zr-in-rutile thermometers. *Contributions to Mineralogy and Petrology* **154**, 429–437.

Frey, H. M. & Lange, R. A. (2011). Phenocryst complexity in andesites and dacites from the Tequila volcanic field, Mexico: resolving the effects of degassing vs. magma mixing. *Contributions to Mineralogy and Petrology* **162**, 415–445.

Garrison, J. M. & Davidson, J. P. (2003). Dubious case for slab melting in the Northern volcanic zone of the Andes. *Geology* **31**, 565–568.

Giacomoni, P. P., Ferlito, C., Coltorti, M., Bonadiman, C. & Lanzafame, G. (2014). Plagioclase as archive of magma ascent dynamics on "open conduit" volcanoes: the 2001–2006 eruptive period at Mt. Etna. *Earth-Science Reviews* **138**, 371–393.

Ginibre, C., Wörner, G. & Kronz, A. (2002). Minor- and trace-element zoning in plagioclase: implications for magma chamber processes at Parinacota volcano, northern Chile. *Contributions to Mineralogy and Petrology* **143**, 300–315.

Ginibre, C., Wörner, G. & Kronz, A. (2007). Crystal zoning as an archive for magma evolution. *Elements* **3**, 261–266.

Giovanni, M. K. (2007) Tectonic and thermal evolution of the Cordillera Blanca detachment system, Peruvian Andes: Implication for normal faulting in a contractionnal orogen. Ph.D. thesis, University of California, Los Angeles, p. 255.

Gutscher, M. A., Olivet, J. L., Aslanian, D., Eissen, J. P. & Maury, R. (1999). The "lost Inca Plateau": cause of flat subduction beneath Peru? *Earth and Planetary Science Letters* **171**, 335–341.

Hammer, J. E. & Rutherford, M. J. (2002). An experimental study of the kinetics of decompression-induced crystallization in silicic melt. *Journal of Geophysical Research: Solid Earth* **107**, ECV 8-1-ECV 8-24.

Harrison, T. M. & Watson, E. B. (1984). The behavior of apatite during crustal anatexis: equilibrium and kinetic considerations. *Geochimica et Cosmochimica Acta* **48**, 1467–1477.

Haschke, M. & Gunther, A. (2003). Balancing crustal thickening in arcs by tectonic vs. magmatic means. *Geology* **31**, 933–936.

Haschke, M., Siebel, W., Günther, A. & Scheuber, E. (2002). Repeated crustal thickening and recycling during the Andean orogeny in north Chile (21–26 S). *Journal of Geophysical Research: Solid Earth* **107**, ECV 6-1-ECV 6-18.

Hattori, K. H. & Keith, J. D. (2001). Contribution of mafic melt to porphyry copper mineralization: evidence from Mount Pinatubo, Philippines, and Bingham Canyon, Utah, USA. *Mineralium Deposita* **36**, 799–806.

Hattori, K. & Sato, H. (1996). Magma evolution recorded in plagioclase zoning in 1991 Pinatubo eruption products. *American Mineralogist* **81**, 982–994.

Hidalgo, S., Monzier, M., Martin, H., Chazot, G., Eissen, J. P. & Cotten, J. (2007). Adakitic magmas in the Ecuadorian volcanic front: petrogenesis of the Iliniza volcanic complex (Ecuador). *Journal of Volcanology and Geothermal Research* **159**, 366–392.

Hidalgo, S., Gerbe, M. C., Martin, H., Samaniego, P. & Bourdon, E. (2012). Role of crustal and slab components in the Northern Volcanic Zone of the Andes (Ecuador) constrained by Sr–Nd–O isotopes. *Lithos* **132**, 180–192.

Hildreth, W. & Moorbath, S. (1988). Crustal contributions to arc magmatism in the Andes of central Chile. *Contributions to Mineralogy and Petrology* **98**, 455–489.

Hollings, P., Cooke, D. R. & Clark, A. (2005). Regional geochemistry of tertiary igneous rocks in central Chile: implications for the geodynamic environment of giant porphyry copper and epithermal gold mineralization. *Economic Geology* **100**, 887–904.

Hou, K. J. (2007). Laser ablation-MC-ICP-MS technique for Hf isotope microanalysis of zircon and its geological applications. *Acta Petrologica Sinica* **23**, 2595–2604.

Hutchinson, M. C. (2019) The nature of sulfate saturation in oxidized arc magmas: implications for magmatic sulfur budgets. Ph.D. thesis, Oregon State University, Corvallis, Oregon, p.189.

Jaillard, E., Hérail, G., Monfret, T., Díaz-Martínez, E., Baby, P., Lavenu, A. & Dumont, J. F. (2000). Tectonic evolution of the Andes of Ecuador, Peru, Bolivia and northernmost Chile. *Tectonic Evolution of South America* **31**, 481–559.

James, J. (1995) Geology, alteration, and mineralization of the Cerro Corona porphyry copper-gold deposit, Cajamarca Province, Peru. B. Sc thesis, University of British Columbia, Vancouver, Canada, p. 266.

Jugo, P. J., Luth, R. W. & Richards, J. P. (2005). An experimental study of the sulfur content in basaltic melts saturated with immiscible sulfide or sulfate liquids at 1300 °C and 1.0 GPa. *Journal of Petrology* **46**, 783–798.

Kay, S. M. & Mpodozis, C. (2001). Central Andean ore deposits linked to evolving shallow subduction systems and thickening crust. *Geological Society of America Today* **11**, 4–9.

Kennan, L. & Pindell, J. L. (2009). Dextral shear, terrane accretion and basin formation in the Northern Andes: best explained by interaction with a Pacific-derived Caribbean Plate? *Geological Society, London, Special Publications* **328**, 487–531.

Kley, J. & Monaldi, C. R. (1998). Tectonic shortening and crustal thickness in the Central Andes: how good is the correlation? *Geology* **26**, 723–726.

Konecke, B. A., Fiege, A., Simon, A. C. & Holtz, F. (2017). Cryptic metasomatism during late-stage lunar magmatism implicated by sulfur in apatite. *Geology* **45**, 739–742.

Konecke, B. A., Fiege, A., Simon, A. C., Linsler, S. & Holtz, F. (2019). An experimental calibration of a sulfur-in-apatite oxybarometer for mafic systems. *Geochimica et Cosmochimica Acta* **265**, 242–258.

Korges, M., Weis, P. & Andersen, C. (2020). The role of incremental magma chamber growth on ore formation in porphyry copper systems. *Earth and Planetary Science Letters* **552**, 116584.

Lange, R. A., Frey, H. M. & Hector, J. (2009). A thermodynamic model for the plagioclase-liquid hygrometer/thermometer. *American Mineralogist* **94**, 494–506.

Le Bas, M. J., Le Maitre, R. W., Streckeisen, A. & Zanettin, B. (1986). A chemical classification of volcanic rocks based on the total alkali-silica diagram. *Journal of Petrology* **27**, 745–750.

Lee, C.-T. A. & Tang, M. (2020). How to make porphyry copper deposits. *Earth and Planetary Science Letters* **529**, 115868.

Li, X. H., Li, W. X., Li, Q. L., Wang, X. C., Liu, Y. & Yang, Y. H. (2010a). Petrogenesis and tectonic significance of the ~850 Ma Gangbian alkaline complex in South China: evidence from in situ zircon U–Pb dating, Hf–O isotopes and whole-rock geochemistry. *Lithos* **114**, 1–15.

Li, X. H., Long, W. G., Li, Q. L., Liu, Y. & Tao, H. (2010b). Penglai zircon megacrysts: a potential new working reference material for microbeam determination of Hf–O isotopes and U–Pb age. *Geostandards & Geoanalytical Research* **34**, 117–134.

Li, X. H., Tang, G. Q., Gong, B., Yang, Y. H., Hou, K. J., Hu, Z. C., Li, Q. L., Liu, Y. & Li, W. X. (2013). Qinghu zircon: a working reference for microbeam analysis of U-Pb age and Hf and O isotopes. *Chinese Science Bulletin* **58**, 4647–4654.

Li, J., Tang, S. H., Zhu, X. K. & Pan, C. X. (2017). Production and certification of the reference material GSB 04-3258-2015 as a ^{143}Nd/^{144}Nd isotope ratio reference. *Geostandards and Geoanalytical Research* **41**, 255–262.

Lin, J., Liu, Y. S., Yang, Y. H. & Hu, Z. C. (2016). Calibration and correction of LA-ICP-MS and LA-MC-ICP-MS analyses for element contents and isotopic ratios. *Solid Earth Sciences* **1**, 5–27.

Litherland, M., Aspden, J. A. & Jemielita, R. A. (1994) The metamorphic belts of Ecuador, British Geological Survey, Overseas Memoir 11. Keyworth: British Geological Survey.

Longo, A. A. (2005) Evolution of volcanism and hydrothermal activity in the Yanacocha mining district, northern Peru. Ph.D. thesis, Oregon State University, Corvallis, USA, p.503.

Longo, A. A., Teal, L., Rhoden, H. N., Steininger, R. C. & Vikre, P. G. (2005). A summary of the volcanic stratigraphy and the geochronology of magmatism and hydrothermal activity in the Yanacocha gold district, northern Peru. *Symposium* 797–808.

Longo, A. A., Dilles, J. H., Grunder, A. L. & Duncan, R. (2010). Evolution of calc-alkaline volcanism and associated hydrothermal gold deposits at Yanacocha, Peru. *Economic Geology* **105**, 1191–1241.

Longridge, J. (2016) Evolution of hydrothermal alteration facies at the Cerro Corona Cu-Au porphyry deposit, Northern Peru. Ph.D. thesis, Imperial College London, London, Britain, p.300.

Lonsdale, P. (2005). Creation of the Cocos and Nazca plates by fission of the Farallon plate. *Tectonophysics* **404**, 237–264.

Loucks, R. R. (2014). Distinctive composition of copper-ore-forming arcmagmas. *Australian Journal of Earth Sciences* **61**, 5–16.

Loucks, R. R. (2021). Deep entrapment of buoyant magmas by orogenic tectonic stress: its role in producing continental crust, adakites, and porphyry copper deposits. *Earth-Science Reviews* **220**, 103744.

Loucks, R. R., Fiorentini, M. L. & Henríquez, G. J. (2020). New magmatic oxybarometer using trace elements in zircon. *Journal of Petrology* **61**, 1–30.

Lu, Y. J., Loucks, R. R., Fiorentini, M., McCuaig, T. C., Evans, N. J., Yang, Z. M., Hou, Z. Q., Kirkland, C. L., Parra-Avila, L. A., Kobussen, A. & Richards, J. P. (2016). Zircon compositions as a pathfinder for porphyry Cu ± Mo ± Au deposits. *Society of Economic Geologists Special Publication* **19**, 329–347.

Luis, R. R. & Julio, C. V. (1987) In: (Tina L., Lomas L., Ayabaca S. A., Morropón H. & y Pomahuaca O. (eds)) *Geología de los Cuadrángulos de Las Playas*, Boletín 39(A). Lima, Peru: Insitituto Geológico, Minero y Metalúrgico.

Luis, R. R. & Julio, C. V. (2017) *Mapa geológico del cuadrángulo de Huancabamba (11-E), escala 1:100,000*. Lima, Peru: Insitituto Geológico, Minero y Metalúrgico.

Lundgaard, K. L. & Tegner, C. (2004). Partitioning of ferric and ferrous iron between plagioclase and silicate melt. *Contributions to Mineralogy and Petrology* **147**, 470–483.

Macfarlane, A. W. (1999). Isotopic studies of northern Andean crustal evolution and ore metal sources. In: Skinner, B.J. (eds) *Geology and Ore Deposits of the Central Andes* **7**, 195–217.

Macpherson, C. G., Dreher, S. T. & Thirlwall, M. F. (2006). Adakites without slab melting: high pressure differentiation of island arc magma, Mindanao, the Philippines. *Earth and Planetary Science Letters* **243**, 581–593.

Maksaev, V., Munizaga, F., McWilliams, M., Fanning, M., Mathur, R., Ruiz, J. & Zentilli, M. (2004). New chronology for El Teniente, Chilean Andes, from U-Pb, $^{40}Ar/^{39}Ar$, Re-Os, and fission-track dating: implications for the evolution of a supergiant porphyry Cu–Mo deposit. *Society of Economic Geologists* **11**, 15–54.

Mamani, M., Carlotto, V., Choquehuanca, S., Santos, A., Rodríguez, J., Cueva, E., Chavez, L., Cereceda, C., Rodríguez, R. & Cacya, L. (2016). *Base de Datos Lithogeoqúimica del Peru, GR4 (INGEMMET)*. Lima, Peru. https://portal.ingemmet.gob.pe/documents/73138/715255/BD_Litogeoquimica_2016_2.xls (accessed 15 November 2021).

Mao, J. W., Luo, M. C., Xie, G. Q., Liu, J. & Wu, S. H. (2014). Basic characteristics and new advances in research and exploration on porphyry copper deposits. *Acta Geologica Sinica* **88**, 2153–2175.

Margirier, A., Robert, X., Audin, L., Gautheron, C., Bernet, M., Hall, S. & Simon-Labric, T. (2015). Slab flattening, magmatism, and surface uplift in the Cordillera Occidental (northern Peru). *Geology* **43**, 1031–1034.

McKee, E. H. & Noble, D. C. (1982). Miocene volcanism and deformation in the western Cordillera and high plateaus of south-central Peru. *Geological Society of America Bulletin* **93**, 657–662.

Mégard, F. (1984). The Andean orogenic period and its major structures in central and northern Peru. *Journal of the Geological Society* **141**, 893–900.

Mégard, F., Noble, D. C., McKEE, E. H. & Bellon, H. (1984). Multiple pulses of Neogene compressive deformation in the Ayacucho intermontane basin, Andes of central Peru. *GSA Bulletin* **95**, 1108–1117.

Meng, X. Y., Kleinsasser, J. M., Richards, J. P., Tapster, S. R., Jugo, P. J., Simon, A. C., Kontak, D. J., Robb, L., Bybee, G. M. & Marsh, J. H. (2021a). Oxidized sulfur-rich arc magmas formed porphyry Cu deposits by 1.88 Ga. *Nature Communications* **12**, 1–9.

Meng, X. Y., Richards, J. P., Kontak, D. J., Simon, A. C., Kleinsasser, J. M., Marsh, J. H., Stern, R. A. & Jugo, P. J. (2021b). Variable modes of formation for tonalite-trondhjemite-granodiorite-diorite (TTG)-related porphyry-type Cu ± Au deposits in the Neoarchean southern Abitibi subprovince (Canada): evidence from petrochronology and oxybarometry. *Journal of Petrology* **62**, egab079.

Michalak, M. J., Hall, S. R., Farber, D. L., Audin, L. & Hourigan, J. K. (2016). (U-Th)/He thermochronology records late Miocene accelerated cooling in the north-central Peruvian Andes. *Lithosphere* **8**, 103–115.

Montgomery, A. T. (2012) Metallogenetic controls on Miocene high-sulphidation epithermal gold mineralization, Alto Chicama district, La Libertad, Northern Peru. Ph.D thesis, Queen's University, Kingston, Canada, p. 436.

Moore, G. & Carmichael, I. (1998). The hydrous phase equilibria (to 3 kbar) of an andesite and basaltic andesite from western Mexico: constraints on water content and conditions of phenocryst growth. *Contributions to Mineralogy and Petrology* **130**, 304–319.

Morel, M., Nebel, O., Nebel-Jacobsen, Y., Miller, J. & Vroon, P. (2008). Hafnium isotope characterization of the GJ-1 zircon reference material by solution and laser-ablation MC-ICPMS. *Chemical Geology* **255**, 231–235.

Mourier, T., Laj, C., Mégard, F., Roperch, P., Mitouard, P. & Medrano, A. F. (1988). An accreted continental terrane in northwestern Peru. *Earth and Planetary Science Letters* **88**, 182–192.

Moyen, J. F. (2009). High Sr/Y and La/Yb ratios: the meaning of the "adakitic signature". *Lithos* **112**, 556–574.

Munoz, M., Charrier, R., Fanning, C., Maksaev, V. & Deckart, K. (2012). Zircon trace element and O–Hf isotope analyses of mineralized intrusions from El Teniente ore deposit, Chilean Andes: constraints on the source and magmatic evolution of porphyry Cu–Mo related magmas. *Journal of Petrology* **53**, 1091–1122.

Mutch, E. J. F., Blundy, J. D., Tattitch, B. C., Cooper, F. J. & Brooker, R. A. (2016). An experimental study of amphibole stability in low-pressure granitic magmas and a revised Al-in-hornblende geobarometer. *Contributions to Mineralogy and Petrology* **171**, 1–27.

Nadeau, O., Williams-Jones, A. E. & Stix, J. (2010). Sulphide magma as a source of metals in arc-related magmatic hydrothermal ore fluids. *Nature Geoscience* **3**, 501–505.

Naney, M. T. (1983). Phase equilibriua of rock-forming ferromagnesian silicates in granitic systems. *American Journal of Science* **283**, 993–1033.

Noble, D. C., McKee, E. H., Mourier, T. & Mégard, F. (1990). Cenozoic stratigraphy, magmatic activity, compressive deformation, and

uplift in northern Peru. *Geological Society of America Bulletin* **102**, 1105–1113.

Parat, F. & Holtz, F. (2004). Sulfur partitioning between apatite and melt and effect of sulfur on apatite solubility at oxidizing conditions. *Contributions to Mineralogy and Petrology* **147**, 201–212.

Parat, F., Holtz, F. & Klügel, A. (2011). S-rich apatite-hosted glass inclusions in xenoliths from La Palma: constraints on the volatile partitioning in evolved alkaline magmas. *Contributions to Mineralogy and Petrology* **162**, 463–478.

Peacock, S. M. (2013) Thermal and petrologic structure of subduction zones. In: (Bebout G. E., Scholl D. W., Kirby S. H. & Platt J. P. (eds)) *Subduction Top to Bottom: Bebout/Subduction Top to Bottom*, Vol. **96**. American Geophysical Union, Washington, D. C., pp.119–133.

Peacock, S. M., Rushmer, T. & Thompson, A. B. (1994). Partial melting of subducting oceanic crust. *Earth and Planetary Science Letters* **121**, 227–244.

Peng, G., Luhr, J. F. & McGee, J. J. (1997). Factors controlling sulfur concentrations in volcanic apatite. *American Mineralogist* **82**, 1210–1224.

Petford, N. & Atherton, M. (1996). Na-rich partial melts from newly underplated basaltic crust: the cordillera Blanca Batholith, Peru. *Journal of Petrology* **37**, 1491–1521.

Petford, N., Atherton, M. P. & Halliday, A. N. (1996). Rapid magma production rates, underplating and remelting in the Andes: isotopic evidence from northern-central Peru (9–11 S). *Journal of South American Earth Sciences* **9**, 69–78.

Piccoli, P. M. & Candela, P. A. (2002). Apatite in igneous systems. *Reviews in Mineralogy and Geochemistry* **48**, 255–292.

Pilatasig, L., Gordón, D., Palacios, O. & Sánchez, J. (2005) *Proyecto multinacional Andino geociencias para las comunidades Andinas-Ecuador-Perú-Canadá*. Lima, Peru: Insitituto Geológico, Minero y Metalúrgico.

Pilger, R. H. (1984). Cenozoic plate kinematics, subduction and magmatism: South American Andes. *Journal of the Geological Society* **141**, 793–802.

Plank, T. (2014) The chemical composition of subducting sediments. In: (Turekian K. K. (ed)) *Treatise on Geochemistry*, 2nd edn. Elsevier, pp.607–629.

Putirka, K. (2016). Amphibole thermometers and barometers for igneous systems and some implications for eruption mechanisms of felsic magmas at arc volcanoes. *American Mineralogist* **101**, 841–858.

Ramos, V. A. (2010). The Grenville-age basement of the Andes. *Journal of South American Earth Sciences* **29**, 77–91.

Reich, M., Parada, M. A., Palacios, C., Dietrich, A., Schultz, F. & Lehmann, B. (2003). Adakite-like signature of Late Miocene intrusions at the Los Pelambres giant porphyry copper deposit in the Andes of central Chile: metallogenic implications. *Mineralium Deposita* **38**, 876–885.

Richards, J. P. (2003). Tectono-magmatic precursors for porphyry Cu-(Mo-Au) deposit formation. *Economic Geology* **98**, 1515–1533.

Richards, J. P. (2011a). High Sr/Y arc magmas and porphyry Cu±Mo±Au deposits: just add water. *Economic Geology* **106**, 1075–1081.

Richards, J. P. (2011b). Magmatic to hydrothermal metal fluxes in convergent and collided margins. *Ore Geology Reviews* **40**, 1–26.

Richards, J. P. (2013). Giant ore deposits formed by optimal alignments and combinations of geological processes. *Nature Geoscience* **6**, 911–916.

Richards, J. P. (2015). The oxidation state, and sulfur and Cu contents of arc magmas: implications for metallogeny. *Lithos* **233**, 27–45.

Richards, J. P. (2018). A shake-up in the porphyry world? *Economic Geology* **113**, 1225–1233.

Richards, J. P. & Kerrich, R. (2007). Special paper: adakite-like rocks: their diverse origins and questionable role in metallogenesis. *Economic Geology* **102**, 537–576.

Richards, J. P., Spell, T., Rameh, E., Razique, A. & Fletcher, T. (2012). High Sr/Y magmas reflect arc maturity, high magmatic water content, and porphyry Cu±Mo±Au potential: examples from the Tethyan arcs of central and eastern Iran and western Pakistan. *Economic Geology* **107**, 295–332.

Ridolfi, F. (2021). Amp-TB2: an updated model for calcic amphibole thermobarometry. *Minerals* **11**, 324.

Ridolfi, F. & Renzulli, A. (2012). Calcic amphiboles in calc-alkaline and alkaline magmas: thermobarometric and chemometric empirical equations valid up to 1,130° C and 2.2 GPa. *Contributions to Mineralogy and Petrology* **163**, 877–895.

Rohrlach, B. D. & Loucks, R. R. (2005) Multi-million-year cyclic ramp-up of volatiles in a lower-crustal magma reservoir trapped below the Tampakan copper–gold deposit by Mio–Pliocene crustal compression in the southern Philippines. In: (Porter T. M. (ed)) *Super Porphyry Copper and Gold Deposits: A Global Perspective*. Adelaide, Australia: PCG Publishing, pp.369–407.

Rollinson, H. R. (2014) *Using Geochemical Data*, Abingdon.

Rosenbaum, G., Giles, D., Saxon, M., Betts, P. G., Weinberg, R. F. & Duboz, C. (2005). Subduction of the Nazca Ridge and the Inca Plateau: insights into the formation of ore deposits in Peru. *Earth and Planetary Science Letters* **239**, 18–32.

Samaniego, P., Martin, H., Monzier, M., Robin, C., Fornari, M., Eissen, J. P. & Cotten, J. (2005). Temporal evolution of magmatism in the Northern Volcanic Zone of the Andes: the geology and petrology of Cayambe Volcanic Complex (Ecuador). *Journal of Petrology* **46**, 2225–2252.

Samaniego, P., Robin, C., Chazot, G., Bourdon, E. & Cotten, J. (2010). Evolving metasomatic agent in the Northern Andean subduction zone, deduced from magma composition of the long-lived Pichincha volcanic complex (Ecuador). *Contributions to Mineralogy and Petrology* **160**, 239–260.

Sandeman, H. A., Clark, A. H. & Farrar, E. (1995). An integrated tectono-magmatic model for the evolution of the southern Peruvian Andes (13-20 S) since 55 Ma. *International Geology Review* **37**, 1039–1073.

Schöpa, A., Annen, C., Dilles, J. H., Sparks, R. S. J. & Blundy, J. D. (2017). Magma emplacement rates and porphyry copper deposits: thermal modeling of the Yerington Batholith, Nevada. *Economic Geology* **112**, 1653–1672.

Schütte, P. (2009) Geochronology, geochemistry, and isotopic composition (Sr, Nd, Pb) of Tertiary porphyry systems in Ecuador. Thesis, University of Geneva, p. 203.

Sillitoe, R. H. (2010). Porphyry copper systems. *Economic Geology* **105**, 3–41.

Sillitoe, R. H. & Perelló, J. (2005). Andean copper province: tectonomagmatic settings, deposit types, metallogeny, exploration, and discovery. *Economic Geology 100th Anniversary Volume* 845–890.

Singer, B. S., Dungan, M. A. & Layne, G. D. (1995). Textures and Sr, Ba, Mg, Fe, K, and Ti compositional profiles in volcanic plagioclase: clues to the dynamics of calc-alkaline magma chambers. *American Mineralogist* **80**, 776–798.

Skewes, M. A. & Stern, C. R. (1994). Tectonic trigger for the formation of late Miocene Cu-rich breccia pipes in the Andes of central Chile. *Geology* **22**, 551–554.

Söderlund, U., Patchett, P. J., Vervoort, J. D. & Isachsen, C. E. (2004). The 176Lu decay constant determined by Lu–Hf and U–Pb isotope

systematics of Precambrian mafic intrusions. *Earth and Planetary Science Letters* **219**, 311–324.

Somoza, R. (1998). Updated Nazca (Farallon)—South America relative motions during the last 40 My: implications for mountain building in the central Andean region. *Journal of South American Earth Sciences* **11**, 211–215.

Somoza, R. & Ghidella, M. E. (2012). Late Cretaceous to recent plate motions in western South America revisited. *Earth and Planetary Science Letters* **331**, 152–163.

Sparks, R. & Marshall, L. (1986). Thermal and mechanical constraints on mixing between mafic and silicic magmas. *Journal of Volcanology and Geothermal Research* **29**, 99–124.

Stern, C. R. & Skewes, M. A. (2005) Origin of giant Miocene and Pliocene Cu–Mo deposits in central Chile: Role of ridge subduction, decreased subduction angle, subduction erosion, crustal thickening and long-lived, batholith sized, open-system magma chambers. In: (Porter T. M. (ed)) *Super Porphyry Copper & Gold Deposits: A Global Perpective*. Adelaide, Australia: PCG Publishing, pp.65–82.

Stern, C. R., Skewes, M. A. & Arévalo, A. (2011). Magmatic evolution of the giant El Teniente Cu–Mo deposit, central Chile. *Journal of Petrology* **52**, 1591–1617.

Streck, M. J. & Dilles, J. H. (1998). Sulfur evolution of oxidized arc magmas as recorded in apatite from a porphyry copper batholith. *Geology* **26**, 523–526.

Sun, S. S. & McDonough, W. F. (1989). Chemical and isotopic systematics ofoceanic basalts: implications for mantle composition and processes. *Geological Society, London, Special Publications* **42**, 313.

Sun, W. D., Ling, M. X., Yang, X. Y., Fan, W. M., Ding, X. & Liang, H. Y. (2010). Ridge subduction and porphyry copper-gold mineralization: an overview. *Science China Earth Sciences* **53**, 475–484.

Tang, M., Lee, C.-T. A., Ji, W. Q., Wang, R. & Costin, G. (2020). Crustal thickening and endogenic oxidation of magmatic sulfur. *Science. Advances* **6**, eaba6342.

Tattitch, B., Chelle-Michou, C., Blundy, J. & Loucks, R. R. (2021). Chemical feedbacks during magma degassing control chlorine partitioning and metal extraction in volcanic arcs. *Nature Communications* **12**, 1774.

Thirlwall, M. (1991). Long-term reproducibility of multicollector Sr and Nd isotope ratio analysis. *Chemical Geology* **94**, 85–104.

Tosdal, R. M. & Richards, J. P. (2001). Magmatic and structural controls on the development of porphyry Cu±Mo±Au deposits. *Structural Controls on Ore Genesis* **14**, 157–181.

Turner, S. J., Langmuir, C. H., Dungan, M. A. & Escrig, S. (2017). The importance of mantle wedge heterogeneity to subduction zone magmatism and the origin of EM1. *Earth and Planetary Science Letters* **472**, 216–228.

Uchida, E., Endo, S. & Makino, M. (2007). Relationship between solidification depth of granitic rocks and formation of hydrothermal ore deposits. *Resource Geology* **57**, 47–56.

Urlich, T. D. (2005) Summary Report on Ar/Ar Dating for MAP: GAC. Activity PE–05 Peru. Vancouver: Laboratory Pacific Centre for Isotopic and Geochemical Research Earth & Ocean Sciences. University of British Columbia.

Ustunisik, G., Kilinc, A. & Nielsen, R. L. (2014). New insights into the processes controlling compositional zoning in plagioclase. *Lithos* **200**, 80–93.

Valley, J. W., Kinny, P. D., Schulze, D. J. & Spicuzza, M. J. (1998). Zircon megacrysts from kimberlite: oxygen isotope variability among mantle melts. *Contributions to Mineralogy and Petrology* **133**, 1–11.

Wang, R., Richards, J. P., Hou, Z. Q., Yang, Z. M., Gou, Z. B. & DuFrane, S. A. (2014). Increasing magmatic oxidation state from paleocene to miocene in the eastern Gangdese Belt, Tibet: implication for collision-related porphyry Cu–Mo±Au mineralization. *Economic Geology* **109**, 1943–1965.

Wang, J. Y., Santosh, M., Yang, C. X., Nakagawa, M. & Dong, Y. (2020). Ancient crustal recycling in modern island arcs: a tale of the world's youngest charnockite from SW Japan. *Lithos* **354**, 105–360.

Waters, L. E. & Lange, R. A. (2015). An updated calibration of the plagioclase-liquid hygrometer-thermometer applicable to basalts through rhyolites. *American Mineralogist* **100**, 2172–2184.

Wieser, P. E., Turner, S. J., Mather, T. A., Pyle, D. M., Savov, I. P. & Orozco, G. (2019). New constraints from Central Chile on the origins of enriched continental compositions in thick-crusted arc magmas. *Geochimica et Cosmochimica Acta* **267**, 51–74.

Wilkinson, J. J. (2013). Triggers for the formation of porphyry ore deposits in magmatic arcs. *Nature Geoscience* **6**, 917–925.

Workman, R. K. & Hart, S. R. (2005). Major and trace element composition of the depleted MORB mantle (DMM). *Earth and Planetary Science Letters* **231**, 53–72.

Wu, F. Y., Yang, Y. H., Xie, L. W., Yang, J. H. & Xu, P. (2006). Hf isotopic compositions of the standard zircons and baddeleyites used in U–Pb geochronology. *Chemical Geology* **234**, 105–126.

Xu, B., Hou, Z. Q., Griffin, W. L., Lu, Y. J., Belousova, E., Xu, J. F. & O'Reilly, S. Y. (2021). Recycled volatiles determine fertility of porphyry deposits in collisional settings. *American Mineralogist* **106**, 656–661.

Zhang, W. & Hu, Z. (2020). Estimation of isotopic reference values for pure materials and geological reference materials. *Atomic Spectroscopy* **41**, 93–102.

Zhang, Q., Qin, K. Z., Zhang, Y., Liu, H. & Wang, Y. (2004). Study on adakite broadened to challenge the Cu and Au exploration in China. *Acta Petrologica Sinica* **20**, 195–204.

Zhang, Z. C., Yan, S. H., Chen, B. L., Zhou, G., He, Y. K., Chai, F. M., He, L. X. & Wan, Y. S. (2006). SHRIMP zircon U-Pb dating for subduction-related granitic rocks in the northern part of east Jungaar, Xinjiang. *Chinese Science Bulletin* **51**, 952–962.

Zhang, Z. C., Mao, J. W., Cai, J. H., Kusky, T. M., Zhou, G., Yan, S. H. & Zhao, L. (2008). Geochemistry of picrites and associated lavas of a Devonian island arc in the northern Junggar terrane, Xinjiang (NW China): implications for petrogenesis, arc mantle sources and tectonic setting. *Lithos* **105**, 379–395.

Zhang, J. B., Wang, R. & Hong, J. (2022). Amphibole fractionation and its potential redox effect on arc crust: evidence from the Kohistan arc cumulates. *American Mineralogist* .

Zhu, J. J., Richards, J. P., Rees, C., Creaser, R., DuFrane, S. A., Locock, A., Petrus, J. A. & Lang, J. (2018). Elevated magmatic sulfur and chlorine contents in ore-forming magmas at the Red Chris porphyry Cu-Au deposit, northern British Columbia, Canada. *Economic Geology* **113**, 1047–1075.